The role of substrate characteristics in producing anomalously young crater retention ages in volcanic deposits on the Moon: Morphology, topography, sub-resolution roughness and mode of emplacement of the Sosigenes Lunar Irregular Mare Patch (IMP)

Le QIAO[1,2,*], James W. HEAD[2], Long XIAO[1], Lionel WILSON[3], and Josef D. DUFEK[4]

[1]Planetary Science Institute, School of Earth Sciences, China University of Geosciences, Wuhan 430074, China.

[2]Department of Earth, Environmental and Planetary Sciences, Brown University, Providence, RI 02912, USA.

[3]Lancaster Environment Centre, Lancaster University, Lancaster LA1 4YQ, UK.

[4]School of Earth and Atmospheric Sciences, Georgia Institute of Technology, Atlanta, Georgia 30332, USA.

[*]Corresponding author E-mail: LeQiao.GEO@gmail.com

Key words: Lunar/Moon, Sosigenes, irregular mare patches, mare volcanism, magmatic foam, lava lake, dike emplacement

Abstract: Lunar Irregular Mare Patches (IMPs) are comprised of dozens of small, distinctive and enigmatic lunar mare features. Characterized by their irregular shapes, well-preserved state of relief, apparent optical immaturity and few superposed impact craters, IMPs are interpreted to have been formed or modified geologically very recently (<~100 Ma; Braden et al. 2014). However, their apparent relatively recent formation/modification dates and emplacement mechanisms are debated. We focus in detail on one of the major IMPs, Sosigenes, located in western Mare Tranquillitatis, and dated by Braden et al. (2014) at ~18 Ma. The Sosigenes IMP occurs on the floor of an elongate pit crater interpreted to represent the surface manifestation of magmatic dike propagation from the lunar mantle during the mare basalt emplacement era billions of years ago. The floor of the pit crater is characterized by three morphological units typical of several other IMPs: 1) bulbous mounds 5–10 m higher than the adjacent floor units, with unusually young crater retention ages, meters thick regolith and slightly smaller sub-resolution roughness than typical mature lunar regolith, 2) a lower hummocky unit mantled by a very thin regolith and significantly smaller sub-resolution roughness, and 3) a lower blocky unit composed of fresh boulder fields with individual meters-scale boulders and rough sub-resolution surface texture. Using new volcanological interpretations for the ascent and eruption of magma in dikes, and dike degassing and extrusion behavior in the final stages of dike closure, we interpret the three units to be related to the late-stage behavior of an ancient dike emplacement event. Following the initial dike emplacement and collapse of the pit crater, the floor of the pit crater was flooded by the latest-stage magma. The low rise rate of the magma in the terminal stages of the dike emplacement event favored flooding of the pit crater floor to form a lava lake, and CO gas bubble coalescence initiated a strombolian phase disrupting the cooling lava lake surface. This phase produced a very rough and highly porous (with both vesicularity and macro-porosity) lava lake surface as the lake surface cooled. In the terminal stage of the eruption, dike closure with no addition of magma from depth caused the last magma reaching shallow levels to produce viscous magmatic foam due to H_2O gas exsolution. This magmatic foam was extruded through cracks in the lava lake crust to produce the bulbous mounds. We interpret all of this activity to have taken place in the terminal stages of the dike emplacement event billions of years ago. We attribute the unusual physical properties of the mounds and floor units (anomalously young ages, unusual morphology, relative immaturity, and blockiness) to be due to the unusual physical properties of the substrate produced during the waning stages of a dike emplacement event in a pit crater. The unique physical properties of the mounds (magmatic foams) and hummocky units (small vesicles and large void space) altered the nature of subsequent impact cratering, regolith development and landscape evolution, inhibiting the typical formation and evolution of superposed impact craters, and maintaining the morphological crispness and optical immaturity. Accounting for the effects of the reduced diameter of craters formed in magmatic foams results in a shift of the crater size-frequency distribution age from less than 100 million years to billions of years, contemporaneous with the surrounding ancient mare basalts. We conclude that extremely young mare basalt eruptions, and resulting modification of lunar thermal evolution models to account for the apparent young ages of the IMPs, are not required. We suggest that other IMP occurrences, both those associated with pit craters atop dikes and those linked to fissure eruptions in the lunar maria, may have had similar ancient origins.

1. Introduction

Lunar Irregular Mare Patches (IMPs) (Braden et al. 2014) are a group of unusual mare features on the Moon, notable for their "blistered" appearance (meniscus-like bulbous shaped mounds with surrounding rough and optically immature materials). Since the discovery of the most notable endogenic IMP feature, Ina, in Lacus Felicitatis (18.65°N, 5.30°E) on Apollo 15 orbiter photographs (Whitaker 1972; El-Baz 1973), lunar IMPs have intrigued lunar scientists for decades. Other major IMP occurrences include Sosigenes in the western margin of Mare Tranquillitatis (Stooke 2012). Sosigenes is also the largest, and most areally extensive among the dozens of IMPs identified on the central nearside (Braden et al. 2014).

The Sosigenes IMP (8.34°N, 19.07°E) was discovered on Lunar Reconnaissance Orbiter Narrow Angle Cameras (LROC NAC) images (Stooke 2012). It is located on the floor of a 7×3 km, approximately elliptical-shaped depression, and is composed of irregularly shaped mounds with surrounding topographically lower, hummocky and blocky units that are typical for other lunar IMP occurrences (Braden et al. 2014). In optical images, the mounds appear to be smoother than the lower units. However, the hummocky and blocky units are more optically immature (e.g., Grice et al. 2016) and have fewer superposed impact craters than the mounds. The wide range of characteristics of the suite of units associated with the Sosigenes IMP floor indicates complex, and potentially different, formation/modification processes for the origin of the multiple interior terrains.

Distinguished by their irregular shapes, well-preserved state of relief, apparent optical immaturity and few superposed impact craters, lunar IMPs are generally regarded to have been formed or modified by geologically recent processes. Crater counts revealed <100 Ma or even younger model ages for Sosigenes and several other lunar IMPs (Braden et al. 2014; Schultz et al. 2006). A topographic diffusional model reported maximum ages of 5–400 Ma for some of the Ina scarps, and suggested that some sub-meter troughs were formed very recently (<1–2 Ma) or are even currently active (Fassett and Thompson 2015).

However, the specific formation mechanism of lunar IMPs has been long debated. Earlier geomorphologic investigations integrated with regional geologic context characterization based on Apollo orbiter photographs suggested that Ina is a collapsed summit caldera of an extrusive volcanic dome, and that the bulbous mounds might represent some of the youngest lava extrusions on the Moon (El-Baz 1973; Strain and El-Baz 1980). Braden et al. (2014) documented 70 small topographic anomalies, with morphologies and textures resembling Sosigenes and other IMPs, on the nearside mare regions, and interpreted the mounds as small lava extrusions that occurred within the last 100 Ma (specifically, ~18 Ma for the Sosigenes mounds), significantly later than the established cessation time of mare basaltic volcanism of ~2.9 Byr ago from isotopic measurements (e.g., Borg et al. 2004), or ~1–1.2 Byr ago from crater size-frequency distribution (CSFD) investigations (Hiesinger et al. 2011; Schultz and Spudis 1983; Head and Wilson 2017).

Recent insights from new orbiter data and terrestrial analogues have provided substantial information on the nature of lunar IMPs with the potential of resolving various issues related to their origin. Observations from LROC NAC data (imagery and topography) and comparative planetology studies of terrestrial lava flow inflation fields (in particular, the McCarty's flow in New Mexico) have led to the proposal that Ina was formed through lava flow inflation processes, in which the mounds were inflated lava flows, the hummocky units were lava breakouts from the margins of the mounds, and the blocky units were boulders exposed through mass wasting processes

(Garry et al. 2012). Radar observations (Carter et al. 2013) revealed that lunar IMPs exhibited a variety of different radar backscatter properties, and that one of the three studied IMPs (Cauchy-5) was mantled by fine-grained, block-free materials, consistent with pyroclastic deposits. Inspired by the same mineralogy between different units within Ina and the background mare deposits (Schultz et al. 2006; Bennett et al. 2015), Bennett et al. (2015) suggested that the mounds and lower units of Ina were probably emplaced contemporaneously and that the significant optical freshness of the lower units was possibly due to their blockiness; however, the specific emplacement mechanism was not indicated and other observed characteristics (e.g., impact crater density) were also not explained. Schultz et al. (2006) examined the optical maturity and superposed impact crater density of the floor rubble terrain at Ina, and proposed that Ina, along with several other IMPs (e.g., Hyginus) were probably volcanic remnants which were at least 3.5 Byr old, but that episodic out-gassing of juvenile volatiles (CO, H_2O) from the deep lunar interior within the past 10 Ma removed the surface regolith materials, causing the rough texture and optical immaturity, and erasing superposed small craters. Thermophysical mapping by the LRO Diviner thermal radiometer revealed that Sosigenes and several other IMPs had much lower rock abundances than the ejecta of some late-Copernican-aged craters (e.g., ~170 Ma Aristarchus and ~85 Ma Tycho, actually only slightly higher than typical lunar surfaces, Ghent et al. 2014) and an interpreted surface regolith layer thicker than 10 cm, suggesting that either lunar IMPs were older than the crater-count dating results, or there was an unusually rapid development of regolith materials on IMPs compared with blocky ejecta blankets (Elder et al. 2016).

Recently, Wilson and Head (2016, 2017b) and Qiao et al. (2016a, 2016b, 2017) proposed that the lunar IMPs are actually ancient in age, contemporaneous with the adjacent mare deposits, and formed through very late stage CO-driven strombolian activity in a lava lake that produced the rough texture of the lower unit and a final H_2O gas exsolution phase that occurred during the final closure of the magmatic dike and produced magmatic foam (very vesicular lava, e.g., Wilson and Head 2017b). The mounds were interpreted by Wilson and Head (2016, 2017b) to have formed from the final stage extrusion of these viscous magmatic foams through fractures in the cooling lake floor. The apparent immaturity of the floor and the meniscus-like shape of the mounds were attributed to very poor crater formation and retention in the mounds and the vesicularity and blockiness of the floor material.

In the present work, in order to explore the formation mechanism of lunar IMPs, we report on an analysis of one of the major IMPs, Sosigenes, based on the latest orbiter data sets. We characterize its regional geologic setting, the morphology and topography of the suite of interior units and the superposed impact craters, and we determine its sub-resolution roughness (with a baseline of centimeters to decimeters) using phase ratio imagery. We then evaluate the several previously proposed formation hypotheses to see if they can account for the observed morphological, topographic, photometric, spectral, and stratigraphic properties observed at Sosigenes and other IMPs. Finally we analyze the applicability to the Sosigenes IMP of the new formation mechanism that was suggested recently based on observations at Ina (Wilson and Head 2016, 2017b; Qiao et al. 2016b, 2017).

2. Data and Methods

We first undertake an analysis of the geomorphological and topographic characteristics of the Sosigenes IMP feature and surrounding region, based on the latest high-resolution orbiter image and altimetric data sets (Figs. 1–11). We use high resolution images (up to 0.47 m pixel size) from LROC NAC to characterize the morphological details of the suite of units associated with Sosigenes. Kaguya Terrain Camera (TC) 10 m/pixel low-sun image mosaics (evening map products, Haruyama et al. 2008) are employed in regional mapping. Topographic and slope analyses are conducted on a 2 m grid Digital Terrain Model (DTM) produced from LROC NAC image pairs (Henriksen et al. 2017). SELENE-TC+LRO-LOLA merged DEM products (SLDEM2015, Barker et al. 2015) are used to characterize regional topographic trends. The SLDEM2015 topography inherits the high spatial sampling resolution of Kaguya TC data (512 pixels/degree (ppd), much higher than raw LOLA data points for non-polar regions), and preserves the excellent altimetric accuracy of the LOLA data (~3–4 m). We also count craters superposed on the Sosigenes mounds using CraterTools in ArcGIS (Kneissl et al. 2011) on LROC NAC images with a range of illumination conditions, and we analyze the crater counting results using the software package CraterStats (Michael and Neukum 2010).

We then use the phase-ratio technique to characterize the surface roughness at sub-resolution scale (Figs. 12, 13 and 15). The brightness (e.g., reflectance, radiance, apparent albedo) of each point on the lunar surface is a function of the phase angle α (e.g., Hapke 2012; Shkuratov et al. 2011). The brightness generally decreases with increasing α, and the rate of this decrease is directly related to the complexity of the surface structure (e.g., roughness and porosity) at the sub-resolution scale. The rate of phase function decrease can be characterized by the phase-ratio technique, which employs two individual images covering the same lunar surface region, but with different phase angles, to generate ratio images. For LROC NAC images with a typical pixel size of ~1 m (Robinson et al. 2010), the derived phase ratio images are sensitive to surface texture with a baseline of centimeters to decimeters. The phase-ratio technique usually can identify many new details, some of which are not well resolved in typical albedo images, e.g., the detection of weak swirls in the southern portion of Oceanus Procellarum (Shkuratov et al. 2010), and has successfully been employed to resolve the origin of some interesting features on the Moon, e.g., dark-halo craters (Kaydash et al. 2014).

To obtain phase ratio images for the Sosigenes IMP, we select LROC NAC frames covering the Sosigenes floor acquired at different phase angles, but with close spatial sampling size and illumination geometry, i.e., similar incidence and sub-solar azimuth angles, thus minimizing the differences in extent and orientation of shadows caused by resolved topographic relief, and aiding the alignment of the image pairs. Imaging conditions of the selected image pair are listed in Table 1.

The raw NAC EDR (Experiment Data Record) images are photometrically corrected and map-projected using the USGS's Integrated Software for Imagers and Spectrometers (ISIS3, e.g., Anderson et al. 2004). The ISIS3 *lronaccal* routine is used to correct the raw NAC image digital number (DN) to radiance factor (f). The NAC radiance factor image pairs are then placed in the same projection, and co-registered with the ISIS3 *coreg* sub-pixel registration routine. The co-registration procedure improves the alignment of the image pairs. The aligned image pairs are finally used to calculate the phase ratio images. In this work, we put the NAC image with smaller-α in the numerator and larger-α in the denominator, which is similar to previous approaches (e.g., Shkuratov et al. 2011; Blewett et al. 2014; Clegg et al. 2014).

3. Results

3.1. Nomenclature

There are multiple features with nomenclatures containing the term *Sosigenes*.

For clarification, we here make a brief reference to the features described in this work (Figs. 1 and 2). *Sosigenes* is the IAU official name for a ~17 km diameter crater centered at 8.7°N, 17.6°E, including three satellite craters, termed *Sosigenes A*, *Sosigenes B*, and *Sosigenes C*. We use the term *Crater Sosigenes* for this ~17 km crater. *Rimae Sosigenes* is the IAU approved term for a lunar rille system, centered at 8.08°N, 18.72°E and near the *Crater Sosigenes*, and we adopt this nomenclature. We here refer to: 1) *Sosigenes depression* or *Sosigenes pit (crater)* as the ~7 km long, elongate depression centered at 8.34°N, 19.06°E; 2) *Sosigenes IMP* as the ~5 km long, irregular mare patch feature on the floor of *Sosigenes pit crater*, centered at 8.34°N, 19.05°E, which consists of the enigmatic Ina-like materials; 3) *Sosigenes linear feature/structure* as a set of co-aligned linear structures, including pit craters, pit chains and linear ridges, centered at 8.25°N, 19.31°E, with a total length of ~33 km.

3.2. Regional geologic setting

The Sosigenes IMP structure is located within an elliptical rimless depression at the western margin of Mare Tranquillitatis, only ~15 km from an adjacent surface of exposures of the ejecta deposit of the Imbrium basin (Fig. 1a-c). This depression is part of a series of three main types of structures (Sosigene linear feature), which co-align in an orientation normal to the strike of the Rimae Sosigenes (Fig. 2), and are radial to the center of Mare Tranquillitatis (Fig. 1). The Sosigenes linear feature clearly cross-cuts one of the Rimae Sosigenes graben, and is thus relatively younger. Nested topographic profiles show that the cross-cut Rima Sosigenes is clearly a graben, with two inward-facing normal faults bounding a down-dropped block (Figs. 2b and 3e). The cross-cut Rima Sosigenes graben is narrowest in the area adjacent to the superposed Sosigenes depression (~0.9 km wide, compared with up to ~1.6 km elsewhere). Rimae Sosigenes are parts of a series of linear and arcuate rilles oriented concentrically to the edge of Mare Tranquillitatis, a common setting around the margins of ancient impact basins. These are attributed to extensional deformation associated with the loading of the impact basins with mare basalts, and associated lithospheric flexure and deformation; the general geometry of loading influences stress orientation and can favor emplacement of dikes, related graben formation above the dikes, and often effusive and explosive eruptions along the strikes of the dike and graben (Solomon and Head 1979, 1980; Head and Wilson 1993). The often discontinuous nature of several of the Rima Sosigenes graben is likely to signal the locations of eruptions and flooded regions from these eruptions; spectral and detrended topographic data showed evidence for numerous lava flows streaming from Rimae Sosigenes down into Mare Tranquillitatis (Tye and Head 2013). Wilson and Head (2017a) and Head and Wilson (1993; 2017) have examined the relationship between dike emplacement and graben formation and have shown that for dikes that stall near the surface, graben formation is a predicted consequence, with variations in dike width along the strike being related to the depth of the top of the dike below the surface; the narrowest part of the graben typically represents the part of the dike closest to the surface, and the graben widens with increasing dike top depth (Head and Wilson 2017). Analysis of the Rima Sosigenes graben shows that it is narrowest in the region of the cross-cutting Sosigenes feature (Figs. 2 and 3e), suggesting that this area represents the top of the dike (Fig. 4).

The younger Sosigenes linear structure itself, about 33 km long, cross-cuts Rima Sosigenes normal to its strike, and has very different features from the graben structure, consisting of co-aligned pit craters, craters aligned in a chain, and a narrow ridge. Two elongate rimless pit craters characterize the western ~12 km of the feature

(Fig. 2). The western-most pit crater is tear-drop shaped, 4.5×2.2 km in dimensions, elongate along strike, and is U-shaped in cross section (Fig. 3a) with a typical floor depth below the rim of ~350 m. It has a volume of ~1.8 km^3. The main feature is an elongate, generally rimless pit crater 7.2×2.8×0.35 km with a relatively flat floor of ~5.1×1.4 km. This pit crater is the deepest part of the series of co-aligned features (315 to 410 m deep; see nested profiles in Fig. 3b), cross-cuts the Rima Sosigenes graben, and has a volume of ~3.8 km^3. The relatively flat floor of this feature is characterized by irregular mare patches (IMPs). The Sosigenes IMP is the most extensive one among the ~70 documented lunar IMP formations (Braden et al. 2014). Extending to the east of this main pit crater is a linear beaded chain of poorly developed coalescing pits, about 6 km long and about 1.5 km wide. The first pit in the chain is the most well-developed and deepest (Fig. 2 and profile #7 in Fig. 3c). These pit chains are very similar to those seen above dikes that reach the shallow subsurface with significant volumes of gas in the dike tip (Fig. 4c) and then partially vent the gas to cause collapse, resulting in subsidence and drainage of material overlying the dike (Head and Wilson 2017; see the case of the Hyginus crater chain, Wilson et al. 2011). The third portion of the feature is a narrow (~0.5 km) discontinuous linear ridge extending about 14–15 km from the eastern end of the pit chain, with a typical height of ~15–20 m (Fig. 3d). This narrow ridge occurs directly along the strike of the center of the feature, and is thus interpreted to be related to the genesis of the collapse pits and crater chain segments. Head and Wilson (2017; their Figs. 14 and 24e) have interpreted similar features elsewhere in the maria to be due to minor lava extrusion during the waning stages of eruptions and the closing of the dike, causing residual magma to be extruded into a narrow ridge.

Taken together, the characteristics of the co-aligned pit craters, pit chains and linear ridge all support the interpretation that these features are related to the intrusion of a dike from the mantle to the shallow subsurface and surface (Fig. 5). The dike intruded normal to Rimae Sosigenes during the basalt filling of Mare Tranquillitatis. We interpret the pit craters and crater chains to be related to the collapse of the gas cavity at the top of the dike, and the ridge to be related to extrusion downslope in the Tranquillitatis basin, formed in the waning stages of dike emplacement and dike closure, as the relatively cooled residual magma in the dike was extruded to the surface (Head and Wilson 2017; their Fig. 16). The extensive void space expected in the subsurface at the top of the dike in this environment provides ample room to accommodate the missing volume from the pit craters and chains due to collapse and drainage. In addition, the pre-existing Rima Sosigenes graben may well have provided additional subsurface void space and have been partly responsible for the relatively larger size and volume of the central flat-floored pit crater. As is common in some lunar collapse pits (e.g., Hyginus; Wilson et al. 2011), the floor of the larger pit may have been resurfaced in the context of the post-collapse closing of the dike and extrusion of basaltic magma onto the pit floor in the same manner that produced the extrusive ridge (Wilson and Head 2017a). This sequence of events is illustrated in Fig. 5.

3.3. Morphology and topography

The enigmatic Ina-like IMP materials occur on the floor of the Sosigenes depression, and are surrounded by depression walls (Fig. 6). The topographic slopes of the depression walls generally range from 15° to 35°, and may achieve a maximum of nearly 50° along some portions of the northern wall (Fig. 7b). The rim of the depression is relatively flat; most areas have a slope less than 2° (baseline is 6 m, Fig.

7b). Unlike Ina, which possesses a low raised "collar" bordering the whole depression (Garry et al. 2012; Strain and El-Baz 1980), the Sosigenes depression only displays a raised rim along a small region on the southern rim, with a maximum height of ~30 m (Figs. 6a, 7a and 7c). Relative to the surrounding mare regions, the Sosigenes depression is ~320 m deep for most of the area of the depression floor, and reaches a maximum depth of ~350 m at the north central margins (Fig. 7a). Within the depression, the regional terrain elevation (Fig. 7) gradually increases by ~50 m from the northern part to southern part over a distance of ~1.3 km, corresponding to a kilometer-scale slope of ~2.2°.

The Sosigenes IMP floor can be categorized in terms of three morphologic units, similar to other lunar IMPs (Garry et al. 2012; Strain and El-Baz 1980; Braden et al. 2014): (1) topographically higher, bulbous-shaped mound units, (2) topographically lower, hummocky units, and (3) topographically lower, blocky units (Fig. 6).

3.3.1. Mound units

The Sosigenes depression floor is dominated by one very extensive and geographically continuous mound unit, with another five smaller mounds (with maximum length <300 m) scattered along the marginal areas of the depression floor (a total of ~82% of the interior floor area, Fig. 6). This association is different from that of Ina, where the mounds are comparable in size with the exposures of the lower terrains, and are composed of over fifty small patches (Garry et al. 2012; Qiao et al. 2016b, 2017). These mound units are typically up to ~10 m higher than the adjacent terrains (Figs. 9 and 10). The margins of the mound units generally have rounded outlines and sharp, scarp-like contacts with the lower hummocky and blocky units (Figs. 9 and 10). Topographic moats, typically ~5 m wide and ~1 m deep, are often observed at the mound-floor contacts (Figs. 10d, e).

Though the mounds appear flat in optical images, their surfaces show a regional topographic trend at longer baselines. The elevation of the mounds is generally higher in the southern and eastern part, lower in the northern regions, and reaches the lowest in the central northern area (Fig. 7a), where the pre-existing Rimae Sosigenes graben intersects (Fig. 6). The total elevation change across the large mound is up to 65 m over 1.2 km distance (Figs. 7 and 8). The topographic pattern of the Sosigenes mounds is significantly different from those of the Ina feature, where the summits of Ina mounds broadly have comparable elevations, and become lower towards the interior; the topographic relief across the Ina mound summits is generally less than 10 m (Garry et al. 2012). The topographic difference between the mounds of Ina and Sosigenes is probably mainly attributed to their geologic settings: the topography surrounding Sosigenes shows a gradual decrease of elevation from western Imbrium ejecta deposits to eastern mare deposits, and the Sosigenes feature intersects some pre-existing linear rilles and wrinkle ridges (Fig. 6), whereas Ina is at the summit of a small shield volcano, with relatively gentle regional topographic relief (Strain and El-Baz 1980; Qiao et al. 2016b, 2017).

Although showing a regional tilt, the surface of the Sosigenes IMP mounds is locally relatively flat: the NAC DTM-derived slope map (with a baseline of 6 m, Fig. 7b) shows that nearly 85% of the mound area has slopes less than 5°. Slopes along the mound margins, however, are typically greater than ~10°, and can reach as high as ~30°. On the relatively steep portions of the mounds, elephant-hide-like texture is observed on the surface regolith (Fig. 11b), which is usually regarded as a result of regolith creep processes (e.g., Melosh 2011).

Some small isolated mounds are present along the peripheral part of the giant mound, though many still show very narrow bridge-like connections with the latter. These marginal mounds are generally more extensive than the other five individual mounds, with a typical dimension of 400×230 m (Fig. 10). These mound units at Sosigenes are typically 5–10 m higher than the adjacent floor units (Figs. 9 and 10), which is systematically less than the Ina mounds (10–20 m, Garry et al. 2012).

The largest impact crater (Fig. 11c) on the Sosigenes mounds has a diameter of ~130 m. The morphological characteristics of this crater, e.g., degraded rim, gentle wall slopes, absence of boulders in the crater interior and surrounding bright rays and halos, suggest this crater is heavily eroded, and massive boulders, if they were initially excavated by the crater-forming impact, have not survived the long period of degradation (boulders breakdown time is estimated at ~300 million years; Basilevsky et al. 2013). Alternatively, the crater may represent an impact into a layer of unconsolidated materials, for instance solidified magmatic foam, in which case it would penetrate deeper and make a smaller crater (Wilson and Head 2016, 2017b). Depth measurements of the freshest craters ≥~20 m in diameter (n=5) on the mounds (Fig. 11a) show that these craters have relatively higher depth/diameter ratios (0.1611 ± 0.0225, 0.1306–0.1828 range) than fresh craters on typical mare basalts (0.096 ± 0.0012, Daubar et al. 2014), suggesting that some regolith materials within these craters may have been crushed as a foam, with maximum impactor penetration.

Some interesting boulder trails are observed to originate from the Sosigenes depression wall and then extend to the depression floor (Figs. 11d, e). Depending on the floor materials, the rolling boulders may have different surface morphological manifestations on the depression floor. A boulder rolling onto the mound units will generally continue to plow through the surface regolith and produce boulder trails until it come to a standstill (Fig. 11d), similar to its behavior observed at the wall. In contrast, a boulder rolling onto the hummocky units will either terminate at the bottom of the wall, or continue to travel on the hummocky unit, but it does not produce any boulder trails detectable on high-resolution LROC NAC images (Fig. 11e). These superposed craters and boulder trail features can provide key information on the regolith properties of different geomorphologic units within the Sosigenes IMP, suggesting relatively thicker regolith (meters thick) on the mound units and much thinner regolith (nearly absent) on the hummocky units (Hovland and Mitchell 1971).

Taken together, the morphologies and dimensions of the Sosigenes mounds and related features all support the interpretation that the mounds have been exposed at the surface for a long period (probably billions of years), and have been modified by subsequent erosion processes.

3.3.2. Hummocky units

The hummocky units generally occur at the margins of the Sosigenes depression floor, although some can extend to the central floor (Fig. 6). The hummocky units along the margins typically have narrow elongate shapes in map view, while those extending to the center regions have irregular and patchy shapes. Compared with the mounds, the total area covered by the hummocky units at Sosigenes is relatively small (~15% by area); this is different from Ina (mounds ~50% and hummocky units ~44%) (Qiao et al. 2016b, 2017). In LROC NAC high resolution images, the hummocky units show ridged and pitted textures (Fig. 11f). The NAC DTM-derived topographic slopes of the hummocky units typically range from 1.5° to 9° (5–95 percentile values); small portions of the hummocky units have surface slopes comparable to those of the mounds (Fig. 7b). The hummocky units generally have scarp-like contacts with the mounds (Fig. 9), and topographic moats are often present along the contacts (Figs.

10d, e). The hummocky units appear rough and angular on high-resolution NAC images; however, very few boulders are observed over most of the hummocky units (Fig. 11g) except for areas surrounding some fresh impact craters.

Some small impact craters are also observed on the hummocky units (Fig. 11g), which can be regarded as natural probes into the shallow subsurface. The diameter of these craters can be as small as ~20 m. However, these small craters still penetrate the surface regolith layers, as massive boulders are excavated and deposited on the crater wall, floor and rim (Fig. 11g). These observations indicate that the surface regolith materials of the hummocky units are very thin, significantly thinner than the excavation depth of these craters (~1.7 m; Melosh 1989). Some irregular depression structures with dimensions up to ~50 m are observed on the hummocky units (Fig. 11f). These depressions are characterized by very complicated geomorphologies, including variable outlines (circular, elliptical, irregular, etc.), concentric interior structures, fractures and mounds on the depression floors. We interpret these depressions to represent poorly developed impact craters, indicating impacts into unusual target materials, e.g., highly-porous solidified lava lake crust.

3.3.3. Blocky units

Blocky units have the smallest areal occurrence among all the three units on the depression floor (3%, compared with 4% for Ina (Qiao et al. 2016b, 2017)) (Fig. 6). These units are mostly observed within the hummocky units or along the edges of hummocky units (Fig. 6). In earlier, relative lower resolution Apollo orbiter photographs, the blocky units at Ina were characterized as “bright” materials (Strain and El-Baz 1980). Images from the LROC NAC with much higher resolution show unambiguously that these units are extensive fresh (thus bright on optical images) boulder fields with individual boulders approaching ~12 m in dimension (Fig. 11h). The surface of these blocky materials is also the most rugged among the three interior units, with slopes ranging from 2° to 13° (5–95 percentile values, Fig. 7b). A large portion of these blocky materials occurs at the contacts between the mounds and hummocky materials, which are characterized by a topographic depression of ~2 m depth (Figs. 9c, d).

3.4. Sub-resolution roughness

Although the LROC NAC images are of very high resolution (~0.47–1.2 m/pixel), additional information on surface morphology and roughness at even higher resolution can be obtained by employing the phase-ratio technique (Kaydash and Shkuratov 2011). Sub-resolution roughness derived from phase-ratio imagery appears to be a very effective tool to study the micro-topography and structure properties of the surface of the Moon and other airless bodies, which is useful for characterizing the nature of surface modification processes, e.g., mass wasting (Kaydash et al. 2012), regolith creep (Kaydash and Shkuratov 2011), pyroclastic deposition (Blewett et al. 2014), and impact melt flows (Shkuratov et al. 2012; Blewett et al. 2014). We here apply the phase-ratio technique to the Sosigenes IMP feature, to see whether it shows any photometric anomalies. The several previously proposed hypotheses for the origin of lunar IMPs make different predictions about the sub-resolution roughness of the IMPs interior materials. The phase-ratio imagery may provide some critical evidence for evaluating these hypotheses.

We calculate phase ratio images of eastern Sosigenes from images acquired at 30° and 67° phase angles (Fig. 12, Table 1). Several image regions of interest (ROIs) are outlined on the mound, hummocky and blocky units, and the surrounding background mature mare regions (Fig. 12c and its raw resolution version in supporting information), to evaluate quantitatively the reflectance and photometric properties of these units. Table 2 presents the average radiance factor and phase ratio values of these ROIs. For all the surfaces of different morphologic units, their radiance factor values in the larger-α image are systematically lower than those in the smaller-α image, which is consistent with the ubiquitous trend of decreasing brightness with increasing phase angle (e.g., Hapke 2012; Jin et al. 2015).

Examination of Fig. 12 and Table 2 reveals both brightness and photometric anomalies for all three morphological units of the Sosigenes IMP. In the smaller-α image ($\alpha = 30°$), the mound units have slightly higher radiance factor values (104%) than the background maria; the hummocky units are significantly brighter (133%) than the background; the blocky units are even brighter than the background mare materials (165%). In larger-α images ($\alpha = 67°$), the mounds have an even higher radiance factor (106%) when compared with the background; the hummocky units are also brighter (158%) than the background; however, the blocky units show a slight decrease in brightness when normalized to the background (159%), though they are still much brighter than background.

Therefore, both the mounds and hummocky units of the Sosigenes IMP exhibit a slower decrease of the radiance factor than the background as the phase angle increases, while the hummocky units show a much slower decreasing trend. However, the blocky units show a contrary photometric trend: a more rapid decreasing of radiance factor than the background with increasing phase angles. These interesting brightness trends with increasing phase angles are clearly demonstrated in the phase ratio ($f(30°)/f(67°)$) images (Fig. 12b and Table 2). The mounds have slightly smaller phase ratio values (~98%), the hummocky units have significantly smaller phase ratio values (~84%), while the blocky units have higher phase ratio values (~107%), than background mature mare regions.

Negative phase ratio anomalies generally correspond to gentler phase function curve slopes largely due to a weakening of the shadow-hiding effect, indicating a smoother sub-resolution surface texture than typical lunar surface regolith materials. Conversely, positive phase ratio anomalies indicate a rougher sub-resolution surface texture. There is a potential correlation between brightness and phase ratio value, which may mislead the evaluation of sub-resolution roughness from phase ratio images. Some previous analyses have observed a positive correlation between the brightness and larger-α/smaller-α phase ratio (Shkuratov et al. 2012). This observed correlation is due to the illumination of the shadows by multiple light scattering from the bright lunar surface. However, no obvious correlation has been observed between the phase-ratio and the radiance factor for the Sosigenes IMP features in this work. The correlation coefficient between $f(67°)/f(30°)$ and $f(30°)$ for eastern Sosigenes (the same extent as Fig. 12) is only 0.2624. The weak correlation is also verified by the two-dimensional scatter plot of phase ratio and radiance factor for the background mare regions and individual terrains of Sosigenes interior (Fig. 13), which clearly shows the very weak correlation of the whole set of plot points, and that the Sosigenes interior terrain units do not generally lie along the trend of the background materials. In addition, a visual check of the brightness and phase ratio images (Fig. 12) can also prove the very weak phase ratio-radiance factor correlation, as we can readily find some areas with close radiance factor values, but significantly different phase ratios. Therefore, the phase ratio image of Sosigenes IMP is a direct and robust indicator of its sub-resolution roughness.

While the hummocky units are often characterized as ‘uneven’ regions, this description is based on meter-scale LROC NAC images (Garry et al. 2012). At sub-resolution length-scales (centimeters or decimeters), the hummocky units are smoother than the mature mare background. We suggest that this is reasonable using evidence from high resolution images. Though the hummocky units appear rugged in meter-scale LROC NAC images, almost no exposed boulders are observed in most portions of the hummocky units (Fig. 11f). The smaller sub-resolution roughness revealed by the phase ratio images is also consistent with the Diviner-derived rock abundance data (Fig. 14, Bandfield et al. 2011). The rock abundance of the hummocky units is not as high as that of the walls of some fresh small craters and the Sosigenes depression wall, where freshly exposed boulders are clearly observed in LROC NAC images. Moreover, the blocky units of the Sosigenes IMP floor indeed have a high concentration of exposed boulders (e.g., central north of Sosigenes, Fig. 11h), which, correspondingly, have greater phase ratio values (Fig. 12b), indicating a rougher sub-resolution surface texture. The consistency among the phase ratio values, LROC NAC images of these blocky materials, and Diviner-derived rock abundance data further validates our sub-resolution roughness interpretations.

The phase ratio images also reveal the confined (i.e., not diffuse) extent of the Sosigenes floor materials, especially for the hummocky units (Fig. 12b). This observation is substantially verified by the phase ratio value profile derived across some of the mounds, hummocky units, and the depression wall at Sosigenes (Fig. 15). The phase ratio profile exhibits a sharp decrease at the margins of the hummocky units (points 2 and 3 in Figs. 12b and 15). One should be aware that the extremely high phase ratio values at the steep scarps of the hummocky unit margins could be artifacts due to resolvable surface topography at the margins. The steep scarps cause significantly different imaging results from different observing angles, which inhibit the alignment of the image pairs (Kaydash et al. 2011), even with similar incidence and sub-solar azimuth angles.

In summary, the LROC NAC phase ratio technique reveals very important characteristics of the Sosigenes IMP interior units: (1) the surface materials of the mound units have slightly smoother sub-resolution surface texture than typical mature lunar mare regolith; (2) the hummocky units are characterized by a significantly lower sub-resolution roughness with confined spatial extent; (3) the blocky units are composed of fresh boulders, with rougher sub-resolution surface texture. These photometric observations will provide key information for analyzing the origin of lunar IMPs.

3.5. Impact crater counts

One of the most unusual characteristics of lunar IMPs is their apparently small number of superposed impact craters, suggesting to Braden et al. (2014) a model age of <100 Ma (specifically, 18.1 Ma for Sosigenes). To explore the potential causes for the extremely low impact crater density, we compile impact crater-size frequency distribution (CSFD) measurements for the Sosigenes IMP. We count all impact craters ≥10 m in diameter on the Sosigenes mounds using LROC NAC images with a range of illuminations geometries (Fig. 16, Table 3). We have taken particular care to eliminate the contamination by secondary impact craters and endogenous pits according to their morphologic characteristics (e.g., Shoemaker 1962; Oberbeck and Morrison 1974; Head and Wilson 2017). To investigate the potential effects of topographic slopes on the density of craters of variable size ranges, we select several typical areas with variable NAC DTM-derived slopes (<3°, 3-6° and >6°, see Fig. 17), count craters with several diameter ranges (10–15 m, 15–20 m, and 20–30 m) and present CSFD (R-values) plots for these areas (Fig. 18 and Table 4). For comparison, we also conducted CSFD and slope analyses on a mare region with similar surface areas (a 2×2 km^2 crater-counting area, and an 840×840 m^2 sub-area for slope analysis) surrounding Sosigenes IMP (Figs. 18-20). The cumulative size frequency distributions of these identified impact craters are plotted in Fig. 21.

Compared with Braden et al. (2014), we identify significantly more impact craters on the Sosigenes mounds, e.g., 683 craters ≥10 m in diameter (compared with 286 of Braden et al. (2014)). The size-frequency distribution of these craters shows partly saturated equilibrium for craters <~35 m in diameter (Fig. 21). Fitting of impact craters ≥35 m yields an absolute model age of 51 ± 10 Ma using the lunar chronology function (CF) and production function (PF) of Neukum et al. (2001), compared with 18.1 ± 1 Ma of Braden et al. (2014).

In addition, the crater density (R-values) at the Sosigenes mounds shows interesting trends with topographic slopes. The R-vale CSFD plot clearly shows that the crater density generally decreases with increasing slope (Fig. 18 and Table 4), indicating that craters on steeper sloped surfaces are more easily destroyed/erased, probably by regolith creep process (Xiao et al. 2013) (although we cannot rule out a statistical error caused by the small size of the count areas (van der Bogert et al. 2015)).

For the 2×2 km^2 mare area south of Sosigenes IMP, we identify 1870 craters ≥10 m in diameter. The production function fit for craters ≥170 m in diameter gives an absolute model age of 2.1 ± 0.9 Ga (Fig. 21), which is younger than the 3.68 (+0.03/-0.04) Ga age reported by Hiesinger et al. (2011) for the surrounding mare regions. We attribute the variability to statistical errors mainly caused by the small count area size (4 km^2), which has been frequently observed in previous studies (e.g., van der Bogert et al. 2015), and the spatially and temporally heterogeneous nature of secondary impacts (e.g., Chapman 2004; McEwen and Bierhaus 2006). Compared with the Sosigenes mounds, typical mare areas are generally very flat (Fig. 20), and show much higher crater densities than the Sosigenes mound areas with comparable slopes (<3°) (Fig. 18).

4. The Origin of Sosigenes IMP Feature

4.1. Evaluation of several previous formation hypotheses

We compile key observations of lunar IMPs from the regional geologic setting (El-Baz 1973; Strain and El-Baz 1980; Garry et al. 2012; and this work), topography (Strain and El-Baz 1980; Garry et al. 2012; Fassett and Thomson 2015; and this work), morphology (Strain and El-Baz 1980; Garry et al. 2012; and this work), sub-resolution roughness (this work), optical maturity (Schultz et al. 2006; Staid et al. 2011; Garry et al. 2013; Bennett et al. 2015), reflectance (Strain and El-Baz 1980; Garry et al. 2013; Staid et al. 2011; and this work), composition/spectroscopy (Bennett et al. 2015; Staid et al. 2011; Schultz et al. 2006), and impact crater density (Schultz et al. 2006; Braden et al. 2014; and this work) to test the several previously proposed formation hypotheses.

4.1.1. Recent individual lava extrusions

Earlier morphologic investigations of Apollo orbiter photographs suggested that the Ina IMP was a collapsed summit caldera of a volcanic dome and, specifically, that the mounds might represent the youngest lava extrusions on the Moon (El-Baz 1973; Strain and El-Baz 1980). Recently, benefiting from the newly-obtained high resolution LROC NAC images, Braden et al. (2014) derived absolute model ages younger than 100 Ma for three IMP occurrences (specifically, ~18.1 Ma for Sosigenes), based on observations from CSFDs, absence of clear crater equilibrium diameters, steep slopes of the mounds' margins (e.g., 8–32° range with average of 16° at Sosigenes), LROC WAC multi-band spectroscopy and NAC morphologies. Specifically, Braden et al. (2014) suggested that the mounds were lava flows emplaced several billion years after the surrounding mare basalts, and that the hummocky units were collapsed eruptive vents (thus fragmenting pre-existing mare deposits within the vents), contemporaneous with the very recent mounds (Fig. 22).

The geologically recent lava extrusion hypothesis, if true, would require a major rethinking of the current and past interior thermal regimes of the Moon as pointed out by Braden et al. (2014). However, a recent volcanic event interpretation cannot explain a range of key observed characteristics. (1) If these mounds are volcanic extrusions emplaced within the last 100 Ma, it is predicted that only a very thin layer of surface regolith would have developed since the very young lava extrusions. Assuming an average regolith accumulation rate of ~1 mm/Myr in the last billion years (Quaide and Oberbeck 1975), the surface regolith developed on the ~18 Ma-aged mare deposits should be significantly thinner than 0.1 m. However, this is inconsistent with regolith thickness estimations for the Sosigenes mounds from (a) observed superposed boulder trails (meters thick, section 3.3.1) and (b) Diviner thermophysical analysis (>0.1 m, Elder et al. 2016). (2) The recent lava extrusion hypothesis also contradicts the absence of excavated boulders on crater walls at the Sosigenes mounds; this absence suggests hundreds of millions years of degradation processes, or impacting into unconsolidated materials, e.g., solidified magmatic foams (section 3.3.1). (3) Additionally, as suggested by Bennett et al. (2015), the recent lava extrusion hypothesis is also inconsistent with the mineralogy (high-Ca pyroxene-dominated) of the different units within Ina and the surrounding mare being the same (Schultz et al. 2006; Bennett et al. 2015), because neither a long-lived magma reservoir nor late-stage magma is likely to have the same mineralogy as the original ancient magma source. The same mineralogy strongly suggests that different units of lunar IMPs are emplaced contemporaneously with the surrounding mare deposits, but may have experienced variable subsequent modification processes. (4) Finally, theoretical and observational treatments of the thermal and tectonic evolution of the Moon demonstrate that the continued net cooling of the Moon decreased the volume of mantle melting, thickened the lithosphere, and caused the global state of stress to be increasingly contractional. All of these factors progressively inhibited the generation, ascent and eruption of basaltic magma (e.g., Head and Wilson 1992; 2017), leading to volcanism having waned in middle lunar history and ceased sometime in the last ~1 Ga, consistent with extensive analyses of returned samples and remote sensing data (e.g., Hiesinger et al. 2011; Morota et al. 2011). It seems very unlikely that lunar extrusive eruptions would have been dormant for over 1 Ga, while became active again very recently (18–58 Ma; Braden et al. 2014).

4.1.2. Lava flow inflation

Based on morphologic and topographic analyses of Ina and terrestrial analogues, Garry et al. (2012) interpreted Ina to resemble some terrestrial inflated lava flows (in particular, the McCarty's flow in New Mexico), mainly in dimensions and topographic relief. Thus, Ina was suggested to be formed by lava flow inflation processes, in which the mounds were inflated lava sheet lobes, the hummocky units were breakouts from the margins of the mounds, and blocky units were fresh surfaces exposed by mass wasting of both units (Fig. 22). The Garry et al. (2012) lava inflation model does not clearly propose a formation age for Ina.

Large volume lava flows on terrestrial bodies commonly experience inflation processes (e.g., Hon et al. 1994); however, inflated terrestrial flows are still dissimilar to lunar IMPs in many aspects, and the lava inflation processes alone cannot readily explain the range of distinctive characteristics of different morphologic units of Sosigenes and other major IMPs that indicate a much more complex set of formation/modification processes for their origin. For example, (1) Garry et al. (2012) showed that the Ina mounds have dimensions and heights comparable to those of inflated lava sheet lobes in the McCarty's flows. The McCarty's inflated flow features are generally spatially connected (e.g., Fig. 8a in Garry et al. 2012), as these flows were initially emplaced as broad sheets of lava, while dozens of spatially separated mounds are mapped out at several IMPs (e.g., Ina (Fig. 2 in Garry et al. 2012), Sosigenes (Fig. 6b)), suggesting they were initially emplaced separately. The McCarty's inflated flows also do not have the roughly elliptical planform outlines of some IMP mounds. (2) No associated source vents have been unambiguously identified in lunar IMPs. Although Garry et al. (2012) suggested that some rimless depressions on the tops of Ina mounds were potential vent features, NAC images obtained under very low sun illuminations (<3°) clearly reveal the rim crest structures of these summit depressions (Fig. 23), indicating that they are more likely to be impact craters. (3) The lava flow inflation hypothesis suggested that all the morphologic units of IMPs (e.g., mound and hummocky units) were emplaced geologically contemporaneously (though they may have developed differently in a stratigraphic sequence); this is inconsistent with the significant differences between the mound and hummocky units in both superposed impact crater density and optical maturity (indicating either a much younger age for the hummocky units than the mounds, or variable formation/modification processes). (4) The lava inflation hypothesis suggested that the blocky units were fresh surfaces exposed by mass wasting processes. However, we find that many blocky units occur on relatively flat regions (with 6-m-basline slope <3°, Figs. 6, 9c, 9d and 17), which is inconsistent with the sloped surface (typically >10°) required for the mass wasting process on the Moon (Xiao et al. 2013). (5) Flow features in the lower units of terrestrial lava flow fields are observed to embay the margins of the higher units (inflated flows), but this is not seen at lunar IMPs, and it actually appears that the mounds embay the hummocky terrain. In summary, we suggest that although lava flow inflation may have played some role in the initial stage of the IMP formation process (Wilson and Head 2016, 2017b; Qiao et al. 2016b, 2017), additional subsequent surface modification processes are required to produce the highly variable characteristics of different units within lunar IMPs, including regolith thickness, sub-resolution roughness, impact crater density, and optical freshness.

4.1.3. Pyroclastic deposits

Radar data showed that lunar IMPs exhibited a range of variable radar backscatter properties. In particular, one of the three studied IMPs (i.e., Cauchy-5) showed unusual low radar circular polarization ratio (CPR) values compared with the background mare, interpreted as mantling by fine-grained and block-free materials (Carter et al. 2013). Carter et al. (2013) thus proposed pyroclastic deposition for the origin of some lunar IMPs. Facilitated by the much higher spatial sampling resolution of LROC NAC images (~1 m) than the radar experiments (80 m for Arecibo S-band data), our phase ratio techniques reveal the confined spatial extent of the finer materials at Sosigenes IMP, which cannot be resolved on relatively coarser radar data sets. However, the gas expansion mechanism that drives explosive eruptions causes them to disperse ash and pyroclasts continuously over a wide area (e.g., Gaddis et al. 2003; Wilson et al. 2015; Blewett et al. 2014). Therefore, we suggest that pyroclastic eruptions are not likely to be responsible for the formation of lunar IMPs, although they may play a role in the initial opening stage of the eruption (Wilson and Head 2016, 2017a; Head and Wilson 2017). Our suggestion is also supported by M^3 spectroscopic observations, which show similar mineralogy for the different morphologic units of IMPs and the surrounding mare basalt deposits, and no detection of glass-bearing materials (Bennett et al. 2015; Grice et al. 2016), which are often observed in M^3 spectroscopic data of pyroclastic deposits (e.g., Jawin et al. 2015).

4.1.4. Out-gassing removal of surface regolith

Schultz et al. (2006) hypothesized another formation process for lunar IMPs, in which the mounds are ancient volcanic features formed at least 3.5 Byr ago, contemporaneous with the surrounding mare basalts, but episodic out-gassing of juvenile volatiles (e.g., CO_2, H_2O) trapped deep in the Moon within the past ~10 Myr removed multiple parts of the surface fine materials, and exposed the underlying long-buried basaltic bedrock, thus forming the lower hummocky/blocky units of IMPs (Fig. 22). However, in a manner similar to explosive volcanic eruptions, out-gassing removal of surface regolith will also generate finer-particle materials with a diffuse extent, which is again inconsistent with our phase ratio observations. LROC NAC sub-resolution roughness investigations of Apollo landing sites, where the surface regolith materials are blown by the gas jets below the lunar descent modules, also show regions of lower sub-resolution roughness with diffuse extent (e.g., Kaydash et al. 2011). The proposed out-gassing events for the origin of IMPs would also rapidly emit gas, thus diffusively smoothing the surface. Therefore, we suggest that recent out-gassing event is also not likely to be the origin of lunar IMPs.

4.2. A new origin for lunar IMPs

As none of the common geological processes discussed above are fully consistent with all the observed characteristics, we here focus on the Sosigenes IMP, and explore the applicability of a new formation mechanism, which was suggested recently based on physical volcanology analyses of late-stage lunar eruptions (Wilson and Head 2016, 2017b) and observations of Ina (Qiao et al. 2016b, 2017), for the Sosigenes IMP. Following the latest assessment on the generation, ascent and eruption of magma on the Moon (Wilson and Head 2016, 2017a; Head and Wilson 2017) and documentation of magmatic-volcanic processes from terrestrial volcanic fields (Qiao et al. 2016b, 2017), we interpret the Sosigenes IMP and related features to be consistent with an origin as the products of the waning stages of an eruption in a linear pit crater atop a dike.

4.2.1. Waning stages of dike-tip pit crater eruptions

During the major phase of lava filling of the Mare Tranquillitatis basin interior, magmatic dikes are emplaced below the basin (Fig. 4a). Among these dozens of dikes developed in the western Tranquillitatis basin, some dikes with sufficient magma overpressure will propagate all the way to the surface and initiate effusive and explosive eruptions along the strike of the dike, as evidenced by the observation of numerous lava flows streaming from western Tranquillitatis down into the basin center (Tye and Head 2013). Some dikes, propagating only into the shallower parts of the crust, can introduce near-surface extensional stress fields above the dike (Fig. 4d), and generate the Rimae Sosigenes graben system, one of which is cross-cut by the Sosigenes depression feature (Fig. 1c). The cross-cut Rima Sosigenes graben is narrowest in the area adjacent to the superposed Sosigenes feature, which typically represents the part of the dike closest to the surface (Fig. 5a). Then, a new gas/foam-filled dike propagates to the shallow subsurface and intrudes normal to Rima Sosigenes (Fig. 5b), but the dike emplacement-generated near-surface stress field is insufficient to cause graben-forming deformation (Fig. 4c). Initially, the magma ascent speed is so great (many tens of m/s) that the gas bubbles (mainly CO) are essentially uniformly distributed in the magma as it approaches the surface. The eruption of these bubbles into the lunar vacuum allows the magma to fragment into sub-mm-sized droplets and gas to expand indefinitely in all directions; this is the lunar equivalent of a relatively steady hawaiian-style eruption (Wilson and Head 2017a, 2017b). The venting of these pyroclastic components causes the collapse, subsidence and drainage of the materials overlaying the dike, forming a series of co-aligned pit craters and crater chains, as observed at the Sosigenes linear features (Fig. 4c), i.e., the Sosigenes depression, the west-most pit craters and the pit chains east of the Sosigenes depression (Fig. 2). As the maximum shallow-subsurface void space is expected at the intersection of the two dike tips, it is very likely that this part of the dike tip would experience the most collapse (Fig. 5c), as evidenced by the deepest part of the Sosigenes depression among the co-aligned linear features (Figs. 2b and 3). Extruded lava from the dike will enter the collapsed Sosigenes pit crater floor, flooding it, and producing a lava lake with a maximum area of ~6 km^2 (Fig. 5). During the terminal stage of dike emplacement outside the pit crater and the closing of the dike, residual magma formed a minor lava extrusion, producing a narrow ridge atop the dike (Head and Wilson 2017), namely the east-most narrow ridges (Fig. 2).

As the excess pressure in the dike is lost, the magma rise speed must decrease and eventually become very small (close to or less than ~1 m/s). The difference between the ascent speed of the magma and the buoyant rise of gas bubbles becomes less, and the prolonged transit time allows bubbles (mainly CO) to coalesce. This leads to a change in eruption style towards strombolian activity, in which large bubbles emerge intermittently through the surface of the overlying lava lake (Fig. 24). During this period, radiative cooling of the lava lake surface begins. Within a period of several months, the lava lake surface crust grows up to several meters thickness, forming a rigid and platy thermal boundary layer (Wilson and Head 2016, 2017b). During lava lake inflation and deflation, the magma continuously degasses and bubbles and foams accumulate below the lava crust; during deflation, the surface crust is locally deformed into pressure ridges. The bubbles formed during the strombolian explosive phase would have updomed the lava lake surface crust, and ejected large (up to meter scale) disrupted lava lake fragments. The fall-back of these ejecta into the cooling lake surface will further deform the lava lake crust (Fig. 24). Taken together, the nature of the lava lake magma (volatile-rich), the evolution of the lava lake surface (inflation, deflation and subsidence) and its subsequent modification (ejecting and deposition of the lava lake fragments) all make the surface topography and the interior structure more porous and complex: the lava lake surface is topographically tilted, with abundant ejecta fragments and ridged and pitted structures; the upper meters of the lava lake crust are characterized by abundant vesicles (micro-vesicular) and meter scale flat blisters (macro-vesicular) (Fig. 24). Furthermore, additional subsurface void space is predicted due to (1) the abundance of vesicles in the uppermost layers of the lava lake due to bubble flotation and (2) subsurface volume decreasing as a result of the thermal contraction and solidification of the lava (Richter and Moore 1966). We interpret the topographically low hummocky/blocky terrain at Sosigenes IMP to originate from the heavily deformed lava lake crust and its associated structures.

In the final stage of the eruptive process (Wilson and Head 2016, 2017b), as the rise speed of the ascending magma slows to zero, no additional magma from deeper (>10 km) will migrate upward, no more CO will be released, and the only gas production in the dike will be the release of water vapor. The final slug or giant bubble of CO that emerges at the surface marks the last strombolian explosion (Fig. 24). The combination of the near-zero magma rise rate and the several hundred ppm water contents typical of many lunar magmas (Saal et al. 2008; Hauri et al. 2011, 2015) allows the water vapor bubble sizes to be small (~20 μm radius) so that surface tension forces enable them to remain stable against the internal gas pressures, and thus to form a water vapor-dominated magmatic foam layer (Fig. 25). The foam can extend for several hundred meters below the surface in the lava lake crust, and have a vesicularity up to ~95% (Wilson and Head 2016, 2017b). As the excess pressure in the dike decreases to zero, the elastic response of the wall rock attempts to close the dike, slowly squeezing the magmatic foam up toward the surface (~1 cm/s) and deforming the growing lava lake crust (Fig. 25). As the overlying crust is already highly fractured, it is very likely that some of the magmatic foam will be extruded out onto the surface, and produce convex mounds (Fig. 25). Calculations by Wilson and Head (2016, 2017b) indicate that the Sosigenes mounds, with characteristic dimensions of ~400×230×8 m (Fig. 10), can be emplaced over a period of ~10 days. It is probable that the vesicles in the upper part of the mound will pop into the vacuum, in a mini-strombolian style, producing a decimeter to meter-thick layer of low-density, finer soil (upper right panel of Fig. 25; Wilson and Head 2017b). The weight of this thin surface layer will protect the foam materials from further disruption. This popped surface foam layer would have smaller particles size than typical lunar mature regolith, producing a smoother sub-resolution surface texture than that of the background mare, consistent with our phase-ratio imagery results (Fig. 12, Table 2). Extrusion of the foam causes central crust subsidence and local flexure of the crust in the immediate vicinity of the foam, enhancing the meniscus-like borders of the mounds and creating marginal moats and depressions (Fig. 25).

In summary, the final product of the waning stages of the eruptive process associated with a pit crater atop a dike is the superposition and solidification of magmatic foam mounds on a lava lake crust characterized by abundant micro- and macro-vesicularity, and overlying a residual highly porous substrate (Fig. 26). These processes are predicted to operate at the time of formation of the pit crater floor billions of years ago, contemporaneous with the major phase of the Mare Tranquillitatis lava filling process (consisting with the high-Ca pyroxene-dominated high-Ti basalt mineralogy of different IMP units and the surrounding maria (Bennett et al. 2015)). This proposed emplacement model stands in stark contrast to emplacement in the last few millions of years (Schultz et al. 2006; Braden et al. 2014). Can these characteristics, predicted from lunar magma ascent and eruption theory, account for the morphologic crispness, optical immaturity and extremely young crater retention ages of the surface of the Sosigenes pit crater?

4.2.2. Post-emplacement impact cratering, regolith formation and landscape evolution

Impact cratering has been widely regarded as one of the most important geological processes on all planetary bodies with a solid surface, especially for bodies with relatively minor endogenic activity, like the Moon. Impact is a ubiquitous process which operates during the entire lifetime of the Moon, and has significant effects on virtually all surface materials and processes, leading to crater formation, regolith development and landscape degradation.

Impact cratering on typical lunar lava deposits is generally characterized by the fracturing, brittle deformation and comminution of the solid bedrock substrate, and excavation and ejection of solid fragments (Fig. 27a). The final products are mainly well-formed, relatively shallow and blocky craters, as ubiquitously observed on the lunar surface, and lateral ejecta materials. Continuous impacting over billions of years builds up a fragmental layer that increases in thickness with time; this layer is the lunar regolith. Surface regoliths that accumulated on ancient mare basalts like those surrounding the Sosigenes IMP (~2–3 Ga, Hiesinger et al. 2011 and section 3.5) have a typical thickness of 4–5 meters (Bart et al. 2011). Steady bombardment of these fragmented components by charged solar and cosmic particles, and by the micrometeorite flux, results in surface optical maturity (McKay et al. 1991; Lucey et al. 2006). Small impacts on the succeeding regolith and lateral mobilization of ejecta will progressively mute the pristine surface topography over time, leading to the degradation of crisp and sharp landforms and boundaries typical of initially-formed lava flows (Soderblom 1970; Fassett and Thompson 2014).

In contrast, impact cratering on a lava lake crust, such as the topographically low hummocky/blocky terrain of Sosigenes IMP, operates in a markedly different style from that on solid lava deposits (Fig. 27b; Wilson and Head 2016, 2017b). The chilled lava lake crust substrate consists of a highly porous medium, both at the micro-vesicular scale and at the macro-porosity scale due to the presence of large voids produced by crust deformation and disruption during the strombolian phase. Underlying this lake crust is solidified foam with a vertical extent of several hundred meters (Fig. 26). Instead of excavating and ejecting the fragmented substrate materials, impacts into this medium would be characterized by (1) permanent crushing and compaction of the target material, (2) a negligible amount of lateral ejection beyond the crater rim, and (3) infiltration of the finer components of the developing regolith into the abundant macro-porosity of the substrate (Fig. 27b). This unusual cratering mechanism will cause craters to be poorly formed, difficult to recognize, and to degrade rapidly (Fig. 11f and section 3.3.2). The continuous regolith infiltration and absence of abundant lateral ejecta changes the landscape evolution from predominantly lateral diffusion (Fassett and Thompson 2014) to predominantly vertical regolith infiltration, serving to maintain the visual freshness of the terrain and its boundaries with the mounds and other landscape features. The constant infiltration of the fine component of the developing regolith into the underlying void space preferentially exposes larger blocks and boulders, and inhibits the vertical accumulation of regolith materials (<~1.7 m or nearly absence) and optical maturation of the substrate (Fig. 27b). The infiltration process also causes mechanical disturbance of the regolith materials, destroying the porous (“fairy castle”) structure of the upmost portion, and resulting in surface smoothing and brightening (Kreslavsky and Shkuratov 2003; Shkuratov et al. 2011; Kaydash et al. 2011), which is consistent with the radiance factor and sub-resolution roughness observations from LROC NAC images (section 3.4). This process is assisted by “seismic sieving”, by which the multiple impacts forming the regolith cause seismic shaking, enhancing the sieving and infiltration of finer regolith components into the void space and eliminating any potential regolith choking issues (Qiao et al. 2016b, 2017). Together, the presence of abundant small vesicles and large void spaces, and the continuous “seismic sieving” process, combine to inhibit surface regolith development, to cause craters to be poorly formed, to maintain the observed topographic relief and optically immaturity, to expose large blocks and boulders, and to smooth the sub-resolution surface textures (Fig. 27b).

The unusual physical properties of the extruded magmatic foam mounds (abundant micro-vesicularity with bulk porosity >75%) make impact cratering processes differ significantly from those on both lava flow surfaces and the pit crater lava lake crust (Fig. 27c). Extensive laboratory experiments (e.g., Housen and Holsapple 2003, 2011; Schultz et al. 2002; Flynn et al., 2010), numerical modeling (e.g., Wünnemann et al. 2006, 2011, 2012) and spacecraft observations at several asteroids interpreted to have porous interiors (e.g., the NEAR spacecraft at asteroid Mathilde, Housen et al. 1999) have shown the significant effect of target porosity on the impact cratering processes. Highly porous targets are known to efficiently absorb impact shock waves, causing a markedly different cratering mechanism, dominated by permanent crushing and compaction of the target materials, rather than excavating and ejecting of the substrate as in typical non-porous targets (Fig. 27c). Regolith development on these porous materials is inhibited, due to dominantly non-blocky craters and the small amount of ejecta material. This unusual cratering mechanism results in enhanced projectile penetration depths, substantially lower ejection velocities, a negligible amount of material ejected beyond the crater rim, and a significant decrease in crater diameter relative to a similar impact into solid basalt or typical regolith. Thus, the successive accumulation of craters on the magmatic foam mounds results in a population of relatively smaller craters, rapid degradation of newly-formed craters, a minimization of lateral transport of regolith, and a finer grain-size compared to impacts in solid basalt/regolith targets (Fig. 27c).

4.2.3. The anomalously young impact crater retention ages of the Sosigenes IMP interior

We interpret the Sosigenes IMP and related features to originate from the waning stages of dike-tip pit crater eruptions billions of years ago, with production of solidified magmatic foam mounds on a lava lake crust characterized by abundant micro- and macro-vesicularity (Fig. 26). How, then, can these unique products and subsequent surface modification processes account for the impact crater density (CSFD) discrepancy, especially in crater retention ages, between the Sosigenes IMP interior terrain (<100 Ma) and the surrounding ancient mare deposits (~2–3 Ga)? We address this issue using three approaches. Firstly, NAC images with a range of illumination geometries permit us to identify more impact craters (section 3.5 and Table 3) than previous approaches (e.g., Braden et al., 2014), suggesting that craters formed on Sosigenes interior terrains are poorly preserved and easily degraded beyond recognition. Secondly, investigations of the distribution of superposed craters as a function of slope on the mounds clearly shows that there are many fewer small craters where slopes exceed 6 degrees than on the flatter part of the mounds (Fig. 18 and Table 4). This slope-related crater modification is consistent with elephant-hide-like textures observed on the mounds (Fig. 11b). Thus, we conclude that the convex shape of the mounds leads to loss of superposed craters as a function of time.

Finally, we ask the question: could the unique physical properties of the magmatic foam substrate be responsible for altering the superposed CSFD compared with what would be expected in normal basalt lava flows (as observed on the surrounding mare deposits; ~2–3 Ga)? Target property variations have been previously invoked to explain the cratering record discrepancies between coeval surface units observed on the Moon (e.g., van der Bogert et al. 2010, 2013, 2017) and

Mars (Dundas et al. 2010). Experimental impacts show that cratering efficiency (excavated mass/projectile mass) on highly porous targets can be readily reduced by two orders of magnitude compared with cratering on low-porosity materials (Poelchau et al. 2013; Schultz et al. 2002). On the basis of these observations, assuming a porosity of 75% for the extruded magmatic foam of the Sosigenes mounds (the average lunar crust porosity was estimated as 12%; Wieczorek et al. 2013), and considering the effect of porosity on the target density, the predicted one hundred-fold decrease in cratering efficiency would result in a factor of three crater diameter decrease. How does this porosity effect on crater size assist us in interpreting the CSFD disparity between the Sosigenes mounds and the surrounding mare areas (Fig. 21)? We scale all the impact craters recognized on the 2×2 km^2 surrounding mare region with a factor of three diameter decrease (Fig. 28). The CSFD of these scaled mare craters is indistinguishable from the Sosigenes mound CSFD at larger diameters, and yields a model age of 60 Ma for craters ≥57 m (1/3 of the equilibrium onset diameter (170 m) of the 2×2 km^2 surrounding mare crater counting area), very close to our model age of the Sosigenes mound (51 Ma).

On the basis of this analysis, we conclude that the discrepancy in the impact CSFD data between the < 100 Ma age obtained by Braden et al. (2014) for the mounds, and the ~2–3 Ga age obtained here for the surrounding ancient mare can be readily explained primarily by the response of the magmatic foam substrate to the reduced formation size of superposed craters.

5. Conclusions

We present a detailed characterization of the geologic context, topography, morphology, sub-resolution roughness and superposed impact craters of one of the major lunar IMP features, Sosigenes, using the most recent orbiter data sets. We assemble key observations from previous literature and this work to evaluate several previously proposed hypotheses for the origin of lunar IMPs.

The wide range of characteristics of the associated interior terrains of the Sosigenes IMP and surrounding mare, including topography, morphology, regolith thickness, sub-resolution roughness, impact crater density, optical maturity and mineralogy, requires complex, and potentially different, formation/modification processes for its origin. None of the several previously proposed lunar IMP formation mechanisms, including recent individual lava extrusions, lava flow inflation, pyroclastic deposits, and out-gassing removal of surface regolith, can fully reproduce all the observed characteristics.

Based on our latest assessments of the generation, ascent and eruption of magma on the Moon and observations of Ina, we interpret the Sosigenes IMP and related floor units to originate as a portion of a subsurface shallow dike collapsed to create the pit crater, followed by flooding of the pit crater floor with a lava lake, formation of a strombolian phase as the lava lake surface cooled, and finally the extrusion, as the dike closed, of magmatic foams through cracks in the lava lake crust to produce the mounds. The final product of the waning stages of the dike-tip eruptive process is therefore the superposition and solidification of magmatic foam mounds on a lava lake crust (hummocky and blocky units) characterized by abundant micro- and macro-vesicularity, and overlying a residual magmatic foam substrate. The unique physical properties of these final products would make the post-emplacement surface modification processes, including meteoritic impacting, regolith development and landscape degradation, markedly different from those on typical solid lava flows or regolith, maintaining the observed topographic relief and optical immaturity and resulting in an anomalously young crater retention age for the Sosigenes pit crater floor. Accounting for the effects of the reduced diameter of craters formed in magmatic foam results in a shift of the CSFD ages from less than 100 million years to billions of years, contemporaneous with the surrounding ancient mare basalts. We conclude that extremely young mare basalt eruptions, and re-evaluation of lunar thermal evolution models, are not required. We interpret other IMP occurrences associated with pit craters atop dikes (e.g., Cauchy-5, Hyginus) and fissure eruptions in the lunar maria (e.g., the small locality in western Mare Tranquillitatis (9.58°N, 25.51°E), IMP #13 in Braden et al. 2014) to have had similar ancient origins.

Acknowledgments

LQ acknowledges Dave Blewett for help on the processing of phase-ratio images. Clark R. Chapman, an anonymous reviewer and the Associate Editor Stuart J. Robbins have provided very helpful comments and suggestions which improved the manuscript. JWH gratefully acknowledges financial support from the NASA Lunar Reconnaissance Orbiter (LRO) Mission, Lunar Orbiter Laser Altimeter (LOLA) Experiment Team (Grants NNX11AK29G and NNX13AO77G), and the NASA Solar System Exploration Research Virtual Institute (SSERVI) grant for Evolution and Environment of Exploration Destinations under cooperative agreement number NNA14AB01A at Brown University. LQ is partially supported by the State Scholarship Fund as a visiting student at Brown University (No. 201406410040). This study was supported by the National Natural Science Foundation of China (No. 41373066).

Reference

Anderson J. A., Sides S. C., Soltesz D. L., Sucharski T. L., and Becker K. J. 2004. Modernization of the Integrated Software for Imagers and Spectrometers (abstract #2039). 35th Lunar and Planetary Science Conference.

Bandfield J. L., Ghent R. R., Vasavada A. R., Paige D. A., Lawrence S. J., and Robinson M. S. 2011. Lunar surface rock abundance and regolith fines temperatures derived from LRO Diviner Radiometer data. *Journal of Geophysical Research* 116:E00H02.

Barker M. K., Mazarico E., Neumann G. A., Zuber M. T., Haruyama J., and Smith D. E. 2016. A new lunar digital elevation model from the Lunar Orbiter Laser Altimeter and SELENE Terrain Camera. *Icarus* 273:346-355.

Bart G. D., Nickerson R. D., Lawder M. T., and Melosh H. J. 2011. Global survey of lunar regolith depths from LROC images. *Icarus* 215:485-490.

Basilevsky A. T., Head J. W., and Horz F. 2013. Survival times of meter-sized boulders on the surface of the Moon. *Planetary and Space Science* 89:118-126.

Bennett K. A., Horgan B. H. N., Bell J. F. III, Meyer H. M., and Robinson M. S. 2015. Moon Mineralogy Mapper investigation of the Ina irregular mare patch (abstract #2646). 46th Lunar and Planetary Science Conference.

Blewett D. T., Levy C. L., Chabot N. L., Denevi B. W., Ernst C. M., and Murchie S. L. 2014. Phase-ratio images of the surface of Mercury: Evidence for differences in sub-resolution texture. *Icarus* 242:142-148.

Borg L. E., Shearer C. K., Asmerom Y., and Papike J. J. 2004. Prolonged KREEP magmatism on the Moon indicated by the youngest dated lunar igneous rock. *Nature* 432: 209-211.

Braden S. E., Stopar J. D., Robinson M. S., Lawrence S. J., van der Bogert C. H., and Hiesinger H. 2014. Evidence for basaltic volcanism on the Moon within the past 100 million years. *Nature Geoscience* 7:787-791.

Carter L. M., Hawke B. R., Garry W. B., Campbell B. A., Giguere T. A., and Bussey D. B. J. 2013. Radar observations of lunar hollow terrain (abstract #2146). 44th Lunar and Planetary Science Conference.

Chapman C. R. 2004. Mars cratering issues: Secondary cratering and End-Noachian degradation (abstract #8028). Second Conference on Early Mars.

Clegg R. N., Jolliff B. L., Robinson M. S., Hapke B. W., and Plescia J. B. 2014. Effects of rocket exhaust on lunar soil reflectance properties. *Icarus* 227:176-194.

Daubar I. J., Atwood ‐ Stone C., Byrne S., McEwen A. S., and Russell P. S. 2014. The morphology of small fresh craters on Mars and the Moon. *Journal of Geophysical Research* 119:2620-2639.

Dundas C. M., Keszthelyi, L. P., Bray, V. J., McEwen, A. S. 2010. Role of material properties in the cratering record of young platy-ridged lava on Mars. *Geophysical Research Letter* 37:L12203.

El-Baz F. 1973. D-caldera: New photographs of a unique feature, In *Apollo 17 Preliminary Science Report, NASA SP-330*. pp. 30-13–30-17.

Elder C. M., Hayne P. O., Ghent R. R., Bandfield J. L., Williams J. P., and Paige D. A. 2016. Regolith formation on young lunar volcanic features (abstract #2785). 47th Lunar and Planetary Science Conference.

Fassett C. I., and Thomson B. J. 2014. Crater degradation on the lunar maria: Topographic diffusion and the rate of erosion on the Moon. *Journal of Geophysical Research* 119:2255-2271.

Fassett C. I. and Thomson B. J. 2015. A landscape evolution perspective on how young is young on the lunar surface (abstract #1120). 46th Lunar and Planetary Science Conference.

Flynn, G. J., Durda, D. D., Minnick, M. A., and Strait, M. M., 2010, Disruption experiments on porous pumice targets: Implications for cratering and disruption of porous asteroids like Mathilde (abstract #3058). 41st Lunar and Planetary Science Conference.

Gaddis L. R., Staid M. I., Tyburczy J. A., Hawke B. R., and Petro N. E. 2003. Compositional analyses of lunar pyroclastic deposits. *Icarus* 161:262-280.

Garry W., Robinson M., Zimbelman J., Bleacher J., Hawke B., Crumpler L., Braden S., and Sato H. 2012. The origin of Ina: Evidence for inflated lava flows on the Moon. *Journal of Geophysical Research* 117:E00H31.

Garry W. B., Hawke B. R., Crites S., Giguere T., and Lucey P. G. 2013. Optical maturity (OMAT) of Ina 'D-Caldera', the Moon (abstract #3058). 44th Lunar and Planetary Science Conference.

Ghent R. R., Hayne P. O., Bandfield J. L., Campbell B. A., Allen C. C., Carter L. M., and Paige D. A. 2014. Constraints on the recent rate of lunar ejecta breakdown and implications for crater ages. *Geology* 42:1059-1062.

Grice J. P., Donaldson Hanna K. L., Bowles N. E., Schultz P. H., and Bennett K. A. 2016.

Investigating young irregular mare patches on the Moon using Moon Mineralogy Mapper observations (abstract #2106). 47th Lunar and Planetary Science Conference.

Hapke, B. 2012. Theory of reflectance and emittance spectroscopy, 2nd ed. Cambridge, UK: Cambridge University Press. 513 p.

Haruyama J., Matsunaga T., Ohtake M., Morota T., Honda C., Yokota Y., Torii M., and Ogawa Y. 2008. Global lunar-surface mapping experiment using the Lunar Imager/Spectrometer on SELENE. *Earth, Planets and Space* 60:243-255.

Hauri E. H., Weinreich T., Saal A. E., Rutherford M. C., and Van Orman J. A. 2011. High Pre-Eruptive Water Contents Preserved in Lunar Melt Inclusions. *Science* 333:213-215.

Hauri E. H., Saal A. E., Rutherford M. J., and Van Orman J. A. 2015. Water in the Moon's interior: Truth and consequences. *Earth and Planetary Science Letters* 409:252-264.

Head J. W. and Wilson L. 1992. Lunar mare volcanism: Stratigraphy, eruption conditions, and the evolution of secondary crusts. *Geochimica et Cosmochimica Acta* 56:2155-2175.

Head J. W. and Wilson L. 1993. Lunar graben formation due to near-surface deformation accompanying dike emplacement. *Planetary and Space Science* 41:719-727.

Head J. W. and Wilson L. 2017. Generation, ascent and eruption of magma on the Moon: New insights into source depths, magma supply, intrusions and effusive/explosive eruptions (Part 2: Predicted emplacement processes and observations). *Icarus* 283:176-223.

Henriksen M. R., Manheim M. R., Burns K. N., Seymour P., Speyerer E. J., Deran A., Boyd A. K., Howington-Kraus E., Rosiek M. R., Archinal B. A., and Robinson M. S. 2017. Extracting accurate and precise topography from LROC narrow angle camera stereo observations. *Icarus* 283:122-137.

Hiesinger H., Head J. W., Wolf U., Jaumann R., and Neukum G. 2011. Ages and stratigraphy of lunar mare basalts: A synthesis. *Geological Society of America Special Papers* 477:1-51.

Hon K., Kauahikaua J., Denlinger R., and Mackay K. 1994. Emplacement and inflation of pahoehoe sheet flows: observations and measurements of active lava flows on Kilauea Volcano, Hawaii. *Geological Society of America Bulletin* 106:351-370.

Housen K. R., Holsapple K. A., and Voss M. E. 1999. Compaction as the origin of the unusual craters on the asteroid Mathilde. *Nature* 402:155-157.

Housen K. R., and Holsapple K. A. 2003. Impact cratering on porous asteroids. *Icarus* 163:102-119.

Housen K. R. and Holsapple K. A. 2011. Ejecta from impact craters. *Icarus* 211: 856-875.

Hovland H. J. and Mitchell. 1971. Mechanics of rolling sphere-soil slope interaction. In *Lunar Surface Engineering Properties Experiment Definition, Volume II of IV, NASA-CR-121045*, pp. 4-23.

Jawin E. R., Kiefer W. S., Fassett C. I., Bussey D. B. J., Cahill J. T. S., Dyar M. D., Lawrence S. J., and Spudis P. D. 2014. The relationship between radar scattering and surface roughness of lunar volcanic features. *Journal of Geophysical Research* 119:2331-2348.

Jin W., Zhang H., Yuan Y., Yang Y., Shkuratov Y. G., Lucey P. G., Kaydash V. G., Zhu M.-H., Xue B., Di K., Xu B., Wan W., Xiao L., and Wang Z. 2015. In situ optical measurements of Chang'E-3 landing site in Mare Imbrium: 2. Photometric properties of the regolith. *Geophysical Research Letters* 42:8312-8319.

Kaydash V. and Shkuratov Y. 2011. Phase-ratio imagery as a tool to study the lunar surface structure: Example of Vallis Schröteri (abstract #1361). 42nd Lunar and Planetary Science Conference.

Kaydash V., Shkuratov Y., Korokhin V., and Videen G. 2011. Photometric anomalies in the Apollo landing sites as seen from the Lunar Reconnaissance Orbiter. *Icarus* 211:89-96.

Kaydash V., Shkuratov Y., and Videen G. 2012. Phase-ratio imagery as a planetary remote-sensing tool. *Journal of Quantitative Spectroscopy and Radiative Transfer* 113:2601-2607.

Kaydash V., Shkuratov Y., and Videen G. 2014. Dark halos and rays of young lunar craters: A new insight into interpretation. *Icarus* 231:22-33.

Kreslavsky M. A., and Shkuratov Y. G. 2003. Photometric anomalies of the lunar surface: Results from Clementine data. *Journal of Geophysical Research* 108:5015

Kneissl T., van Gasselt S., and Neukum G. 2011. Map-projection-independent crater size-frequency determination in GIS environments—New software tool for ArcGIS. *Planetary and Space Science* 59:1243-1254.

Lucey P., Korotev R. L., Gillis J. J., Taylor L. A., Lawrence D., Campbell B. A., Elphic R., Feldman B., Hood L. L., and Hunten D. 2006. Understanding the lunar surface and space-moon interactions. *Reviews in Mineralogy and Geochemistry* 60:83-219.

McEwen A. S. and Bierhaus E. B. 2006. The importance of secondary cratering to age constraints on planetary surfaces. *Annual Review of Earth and Planetary Sciences*, 34:535-567.

McKay D. S., Heiken G., Basu A., Blanford G., Simon S., Reedy R., French B. M., and Papike J. 1991. The lunar regolith. In *Lunar sourcebook: A user's guide to the Moon*, edited by Heiken G., Vaniman D., and French B. M. Cambridge, UK: Cambridge University Press. pp. 285-356.

Melosh H. J. 1989. Impact cratering: A geologic process, London: Oxford University Press, London.

Melosh H. J. 2011. Planetary surface processes, Cambridge, UK: Cambridge University Press. pp. 319-323.

Neukum G., Ivanov B. A., and Hartmann W. K. 2001. Cratering records in the inner solar system in relation to the lunar reference system. *Space Science Reviews* 96:55-86.

Michael G. G. and Neukum G. 2010. Planetary surface dating from crater size-frequency distribution measurements: Partial resurfacing events and statistical age uncertainty. *Earth and Planetary Science Letters* 294:223-229.

Morota T., Haruyama J., Ohtake M., Matsunaga T., Honda C., Yokota Y., Kimura J., Ogawa Y., Hirata N., Demura H., Iwasaki A., Sugihara T., Saiki K., Nakamura R., Kobayashi S., Ishihara Y., Takeda H., and Hiesinger H. 2011. Timing and characteristics of the latest mare eruption on the Moon. *Earth and Planetary Science Letters* 302:255-266.

Oberbeck V. and Morrison R. 1974. Laboratory simulation of the herringbone pattern associated with lunar secondary crater chains. *The Moon* 9:415-455.

Poelchau M. H., Kenkmann T., Thoma K., Hoerth T., Dufresne A., and SchÄFer F. 2013. The MEMIN research unit: Scaling impact cratering experiments in porous sandstones. *Meteoritics & Planetary Science* 48:8-22.

Qiao L., Head J. W., Xiao L., Wilson L., and Dufek J. 2016a. Sosigenes lunar irregular mare patch (IMP): Morphology, topography, sub-resolution roughness and implications for origin (abstract #2002). 47th Lunar and Planetary Science Conference.

Qiao L., Head J. W., Wilson L., Xiao L. and Dufek J. 2016b. Ina pit crater: Origin as a drained summit lava lake and magmatic foam extrusions modified by seismic sieving (abstract # 7MS3-PS-11). 7th Moscow Solar System Symposium.

Qiao L., Head J., Wilson L., Xiao L., Kreslavsky M., and Dufek J. 2017. Ina pit crater on the Moon: Extrusion of waning-stage lava lake magmatic foam results in extremely young crater retention ages. *Geology* 45:455-458.

Quaide W., and Oberbeck V. 1975. Development of the mare regolith: Some model considerations. *The Moon* 13:27-55.

Richter, D.H. and Moore, J.G. 1966. Petrology of the Kilauea Iki lava lake, Hawaii. USGS Professional Paper 537-B, pp. B1–B26.

Robinson M. S., Brylow S. M., Tschimmel M., Humm D., Lawrence S. J., Thomas P. C., Denevi B. W., Bowman-Cisneros E., Zerr J., Ravine M. A., Caplinger M. A., Ghaemi F. T., Schaffner J. A., Malin M. C., Mahanti P., Bartels A., Anderson J., Tran T. N., Eliason E. M., McEwen A. S., Turtle E., Jolliff B. L., and Hiesinger H. 2010. Lunar Reconnaissance Orbiter Camera (LROC) Instrument Overview. *Space Science Reviews* 150:81-124.

Saal A. E., Hauri E. H., Cascio M. L., Van Orman J. A., Rutherford M. C., and Cooper R. F. 2008. Volatile content of lunar volcanic glasses and the presence of water in the Moon's interior. *Nature* 454:192-195.

Schultz P. and Spudis P. 1983. Beginning and end of lunar mare volcanism. *Nature* 302:233-236.

Schultz P. H., Anderson J. L. B., and Heineck J. T., 2002. Impact crater size and evolution: Expectations for Deep Impact (abstract #1875). 33rd Lunar and Planetary Science Conference.

Schultz P. H., Staid M. I., and Pieters C. M. 2006. Lunar activity from recent gas release. *Nature* 444:184-186.

Shkuratov Y., Kaydash V., Gerasimenko S., Opanasenko N., Velikodsky Y., Korokhin V., Videen G., and Pieters C. 2010. Probable swirls detected as photometric anomalies in Oceanus Procellarum. *Icarus* 208:20-30.

Shkuratov Y., Kaydash V., Korokhin V., Velikodsky Y., Opanasenko N., and Videen G. 2011. Optical measurements of the Moon as a tool to study its surface. *Planetary and Space Science* 59:1326-1371.

Shkuratov Y., Kaydash V., and Videen G. 2012. The lunar crater Giordano Bruno as seen with optical roughness imagery. *Icarus* 218:525-533.

Shoemaker E. M. 1962. Interpretation of lunar craters. In *Physics and astronomy of the Moon*, edited by Kopal Z. New York: Academic Press. pp. 283-360.

Soderblom L. A. 1970. A model for small-impact erosion applied to the lunar surface. *Journal of Geophysical Research* 75:2655-2661.

Solomon S. C., and Head J. W. 1979. Vertical movement in mare basins: Relation to mare emplacement, basin tectonics, and lunar thermal history. *Journal of Geophysical Research* 84:1667-1682.

Solomon S. C., and Head J. W. 1980. Lunar Mascon Basins: Lava filling, tectonics, and evolution of the lithosphere. *Reviews of Geophysics* 18:107-141.

Staid M., Isaacson P., Petro N., Boardman J., Pieters C. M., Head J. W., Sunshine J., Donaldson Hanna K., and Taylor L. A. 2011. The spectral properties of Ina: New observations from the Moon Mineralogy Mapper (abstract #2499). 42nd Lunar and Planetary Science Conference.

Stooke P. J. 2012. Lunar meniscus hollows (abstract #1011), 43rd Lunar and Planetary Science Conference.

Strain P. L. and El-Baz F. 1980. The geology and morphology of Ina. Proceedings, 11th Lunar and Planetary Science Conference, pp. 2437-2446.

Trask, N. J. 1966. Size and spatial distribution of craters estimated from the Ranger photographs, In Ranger VIII and IX, Part II, Experimenters' Analyses and Interpretations, *JPL Technical Reports 32-800*, pp. 252-264.

Tye A. R. and Head J. W. 2013. Mare Tranquillitatis: Distribution of mare domes, relation to broad mare rise, and evidence of a previously unrecognized basin from LOLA altimetric data (abstract #1319). 44th Lunar and Planetary Science Conference.

van der Bogert C. H., Hiesinger H., McEwen A. S., Dundas C., Bray V., Robinson M. S., Plescia J. B., Reiss D., Klemm K., and Team L. 2010. Discrepancies between crater size-frequency distributions on ejecta and impact melt pools at lunar craters: An effect of differing target properties? (abstract #2165). 41st Lunar and Planetary Science Conference.

van der Bogert C. H., Hiesinger H., Krüger T., McEwen A. S., and Dundas C. 2013. New evidence for target property influence on crater size-frequency distribution measurements (abstract #1962). 44th Lunar and Planetary Science Conference.

van der Bogert C. H., Michael G., Kneissl T., Hiesinger H., and Pasckert J. H. 2015. Effects of count area size on absolute model ages derived from random crater size-frequency distributions (abstract #1742). 46th Lunar and Planetary Science Conference.

van der Bogert C. H., Hiesinger H., Dundas C. M., Krüger T., McEwen A. S., Zanetti M., and Robinson M. S. 2017. Origin of discrepancies between crater size-frequency distributions of coeval lunar geologic units via target property contrasts. *Icarus*, in press, doi: 10.1016/j.icarus.2016.11.040.

Whitaker E. A. 1972. An unusual mare feature, In *Apollo 15 Preliminary Science Report, NASA SP-289*. pp. 25-84–25-85.

Wieczorek M. A., Neumann G. A., Nimmo F., Kiefer W. S., Taylor G. J., Melosh H. J., Phillips R. J., Solomon S. C., Andrews-Hanna J. C., and Asmar S. W. 2013. The crust of the Moon as seen by GRAIL. *Science* 339:671-675.

Wilson L., Hawke B. R., Giguere T. A., and Petrycki E. R. 2011. An igneous origin for Rima

Hyginus and Hyginus crater on the Moon. *Icarus* 215:584-595.

Wilson L. and Head J.W. 2016. Three-stage eruption in lunar shield volcanos and the productions of magmatic foam (abstract #7MS3-MN-08). 7th Moscow Solar System Symposium.

Wilson, L. and Head J. W. 2017a. Generation, ascent and eruption of magma on the Moon: New insights into source depths, magma supply, intrusions and effusive/explosive eruptions (Part 1: Theory). *Icarus* 283: 146-175.

Wilson, L., Head, J. W. 2017b. Eruption of magmatic foams on the moon: Formation in the waning stages of dike emplacement events as an explanation of "irregular mare patches". *Journal of Volcanology and Geothermal Research 335:113-127*.

Wilson J. T., Eke V. R., Massey R. J., Elphic R. C., Jolliff B. L., Lawrence D. J., Llewellin E. W., McElwaine J. N., and Teodoro L. F. A. 2015. Evidence for explosive silicic volcanism on the Moon from the extended distribution of thorium near the Compton-Belkovich Volcanic Complex. *Journal of Geophysical Research* 120:92-108.

Wünnemann K., Collins G. S., and Melosh H. J. 2006. A strain-based porosity model for use in hydrocode simulations of impacts and implications for transient crater growth in porous targets. *Icarus* 180:514-527.

Wünnemann K., Nowka D., Collins G. S., Elbeshausen D., and Bierhaus M. 2011. Scaling of impact crater formation on planetary surfaces – Insights from numerical modeling, In Proceedings of the 11th Hypervelocity Impact Symposium, Fraunhofer, Freiburg, Germany. pp. 1-16.

Wünnemann K., Marchi S., Nowka D., and Michel P. 2012. The effect of target properties on impact crater scaling and the lunar crater chronology (abstract #1805). 43rd Lunar and Planetary Science Conference.

Xiao Z., Zeng Z., Ding N., and Molaro J. 2013. Mass wasting features on the Moon – how active is the lunar surface? *Earth and Planetary Science Letters* 376:1-11.

Tables:

Table 1. Characteristics of the LROC NAC images used for phase ratio calculations of Sosigenes IMP.

Image ID	Orbit #	Resolution (m/pixel)	Incidence angle (°)	Emission angle (°)	Phase angle (°)	Sub-solar azimuth (°)	Center latitude (°)	Center longitude (°)
M1129354261R	18571	1.174	45.95	21.25	67.01	190.93	8.33	19.07
M1175290064L	25030	1.104	45.99	15.96	30.27	187.82	8.3	19.11

Table 2. Mean values with one standard deviation of radiance factor and phase ratio for the image regions of interest (ROIs) of Sosigenes (see Fig. 12c). The values in brackets are multiples scaled to the background values.

ROI	Radiance factor in $\alpha = 30°$ image	Radiance factor in $\alpha = 67°$ image	Phase ratio $f(30°)/f(67°)$
Mound unit	0.0315 ± 0.0012 (1.0430)	0.0208 ± 0.0011 (1.0612)	1.5157 ± 0.0334 (0.9819)
Hummocky unit	0.0402 ± 0.0042 (1.3311)	0.0310 ± 0.0032 (1.5816)	1.2972 ± 0.0601 (0.8404)
Blocky unit	0.0499 ± 0.0074 (1.6523)	0.0311 ± 0.0058 (1.5867)	1.6546 ± 0.4732 (1.0719)
Background	0.0302±0.0017	0.0196±0.0015	1.5436±0.0452

Table 3. Information on the crater counts performed on the Sosigenes mounds (Fig. 16) and surrounding 2×2 km^2 mare area (Fig. 19).

Count area	Size of counting area (km^2)	# of craters D ≥10 m	# of craters D ≥25 m	# of craters D ≥50 m
Sosigenes mounds	4.46	683	47	5
Surrounding mare	3.96	1870	212	54

Table 4. Crater statistics results for representatively-sloped areas in Sosigenes mounds and surrounding mare, with variable crater diameter (D) range. See Figs. 16 and 19 for full crater count map, and Figs. 17 and 20 for the areas studied.

Areas	Flat	Median-sloped	Steep	Mare
NAC DTM Slope (°)	1.8±1.2	4.3±1.3	8.9±3.1	2.8±2.3
Area (km^2)	0.69	0.33	0.20	0.71
# of craters ≥10 m	190	34	11	339
D: 10–15 m				
# of craters	140	26	9	236
R-value	0.0745	0.0287	0.0146	0.1229
D: 15–20 m				
# of craters	31	6	1	48
R-value	0.0466	0.0187	0.0046	0.0707
D: 20–30 m				
# of craters	12	1	0	36
R-value	0.0255	0.0044	0.0000	0.0750

Figures:

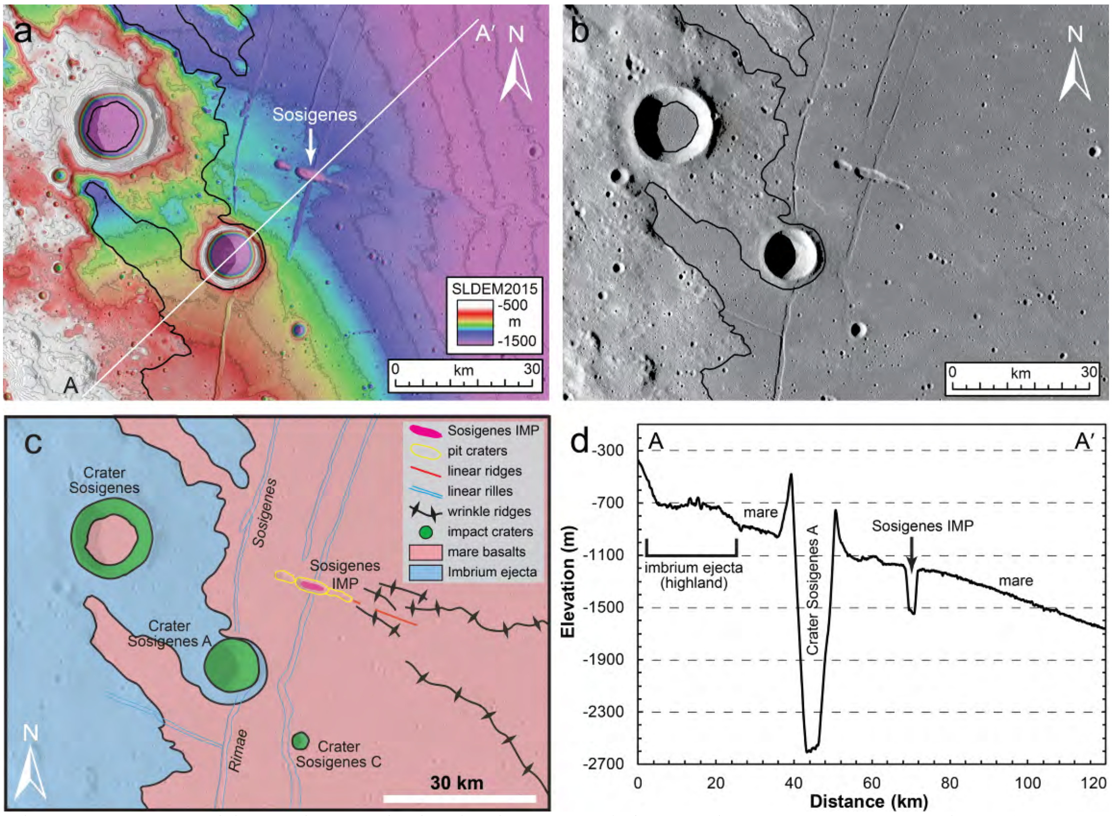

Fig. 1. Topographic and morphological maps of the Sosigenes context region. (a) SLDEM2015 512 ppd grid topography overlain on Kaguya TC evening mosaic. The black lines indicate the boundary of mare regions, and the white line marks the location of the topographic profile in (d). Contour interval is 100 m. (b) Kaguya TC evening mosaic, spatial resolution is ~10 m/pixel. (c) Sketch map of the geologic context of the Sosigenes IMP feature. (d) Topographic cross-section profile from SLDEM2015 gridded DTM shown in (a). All the maps for the Sosigenes region in this paper are projected into sinusoidal projection with a central meridian of 19.0883°E, and north is up.

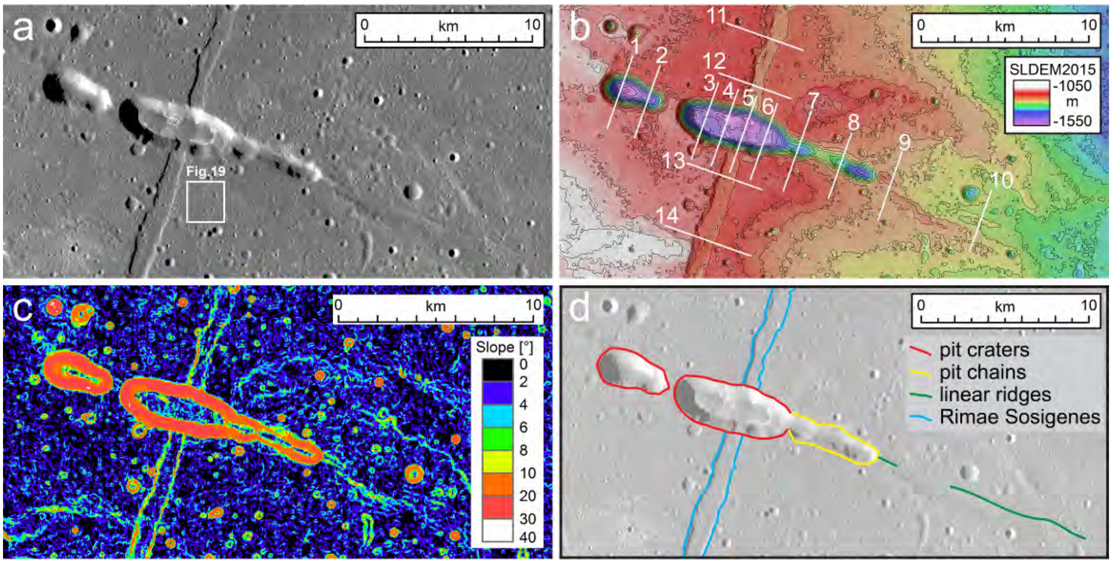

Fig. 2. Maps of the Sosigenes linear feature and one of the Rimae Sosigenes graben: (a) Kaguya TC evening mosaic; extent of Fig. 19 is marked by the white box, (b) SLDEM2015 512 ppd grid topography overlain on Kaguya TC evening mosaic; locations of topographic profiles in Fig. 3 are marked by white lines, with their starting points labeled by the profile numbers, and contour interval is 25 m, (c) SLDEM2015 topographic slope map, and (d) sketch geologic map, with boundaries of Sosigenes linear feature and Rimae Sosigenes marked by lines of different colors.

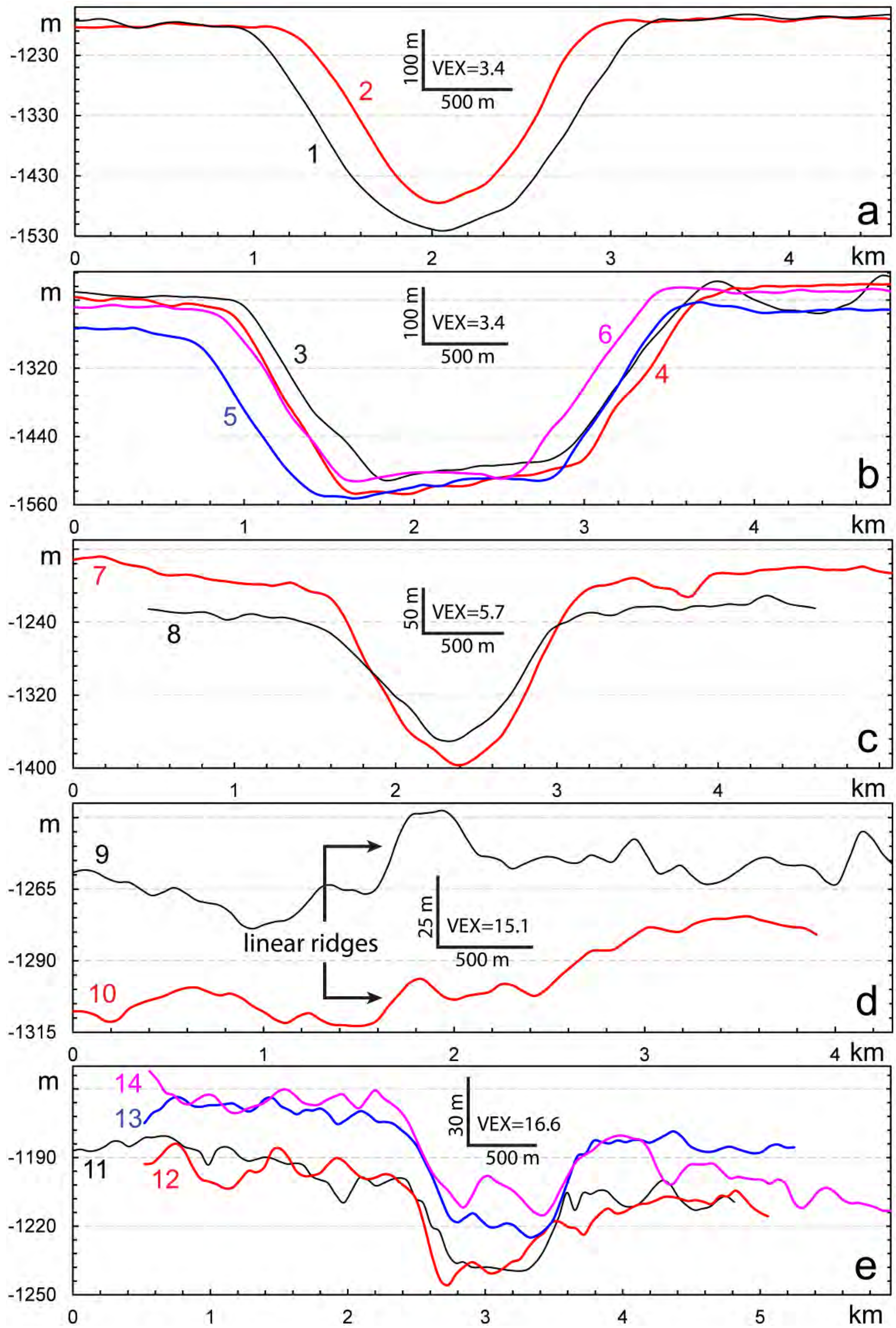

Fig. 3. Stacked topographic profiles of the Sosigenes linear features and one of the Rimae Sosigenes graben derived from SLDEM2015 topography: (a) western-most pit crater, (b) Sosigenes depression, (c) eastern crater chain, (d) eastern-most linear ridge and (e) N-S trending Rimae Sosigenes graben. The horizontal axes are distances in kilometers, and vertical axes are elevations in meters. The locations of these profiles are shown in Fig. 2b, and the profile numbers correspond to those shown there.

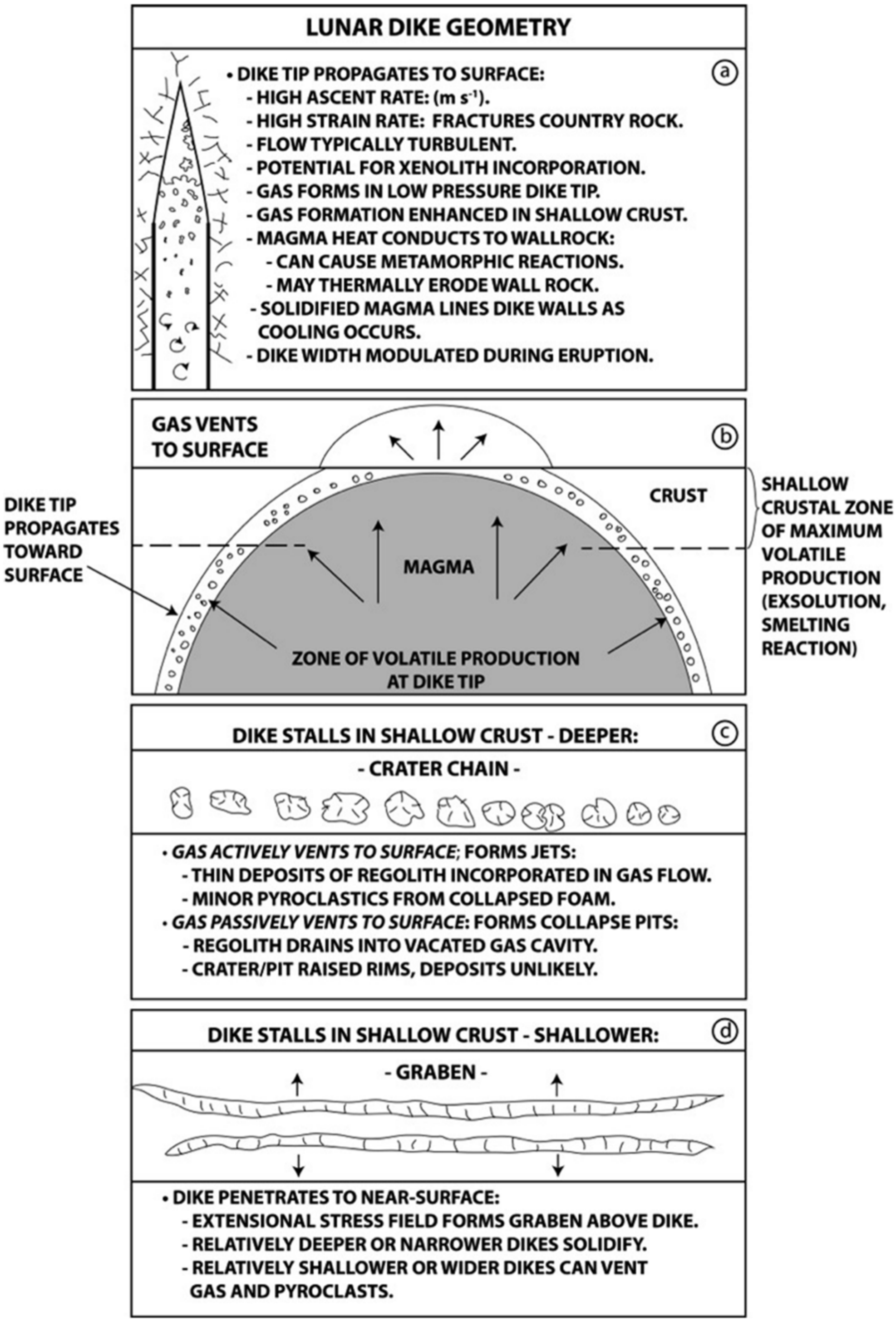

Fig. 4. Block diagrams (from Fig. 6 in Head and Wilson 2017) illustrating lunar dike propagation processes and associated surface manifestation: (a) general lunar dike geometry, (b) processes at the dike tip, (c) dike stalls in shallower crust, resulting in crater chains at the surface, and (d) dikes stall in shallow subsurface, resulting in graben.

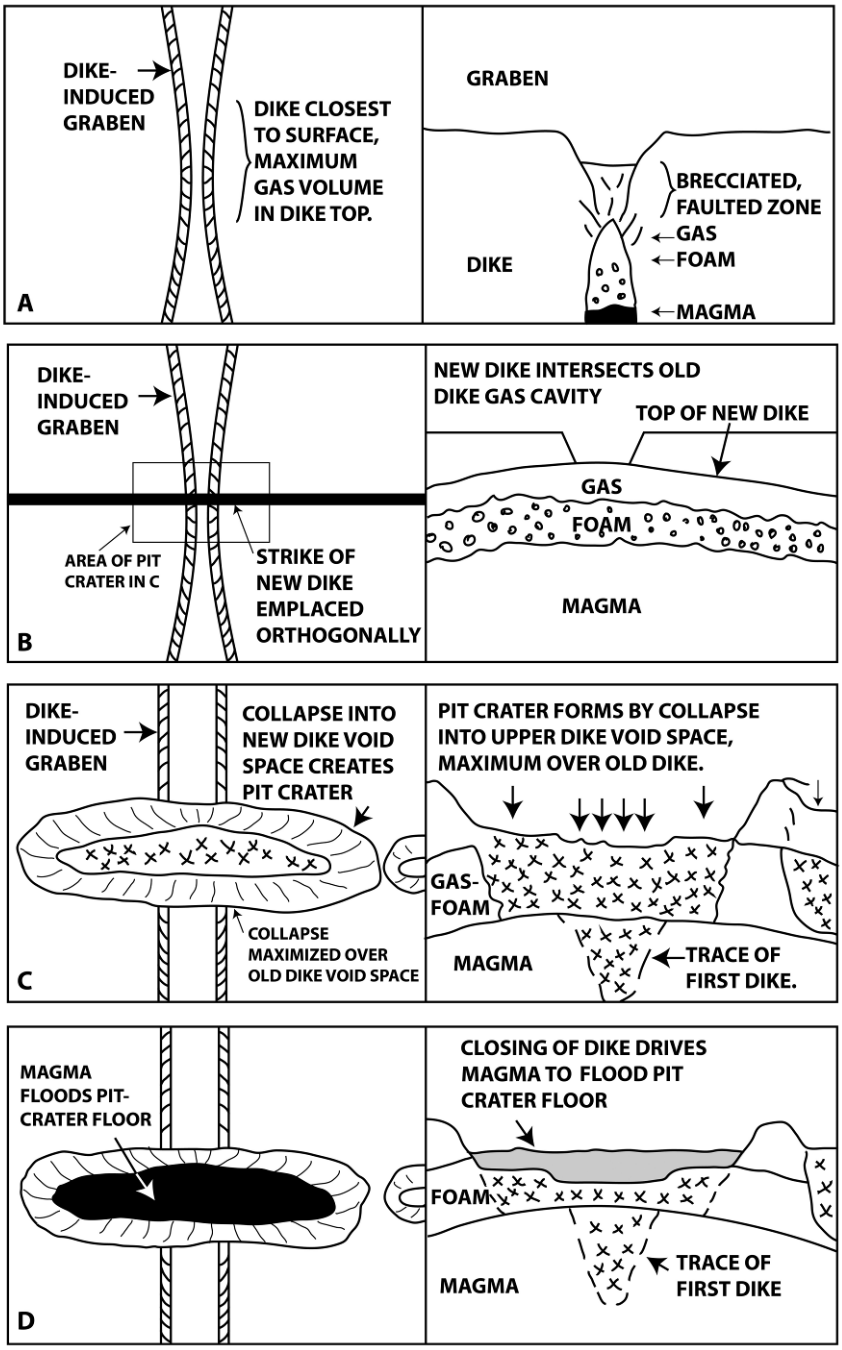

1359
1360 Fig. 5. Interpretative diagram for formation of Sosigenes linear features and Rimae
1361 Sosigenes graben. Left column, map view; right column, cross section view.

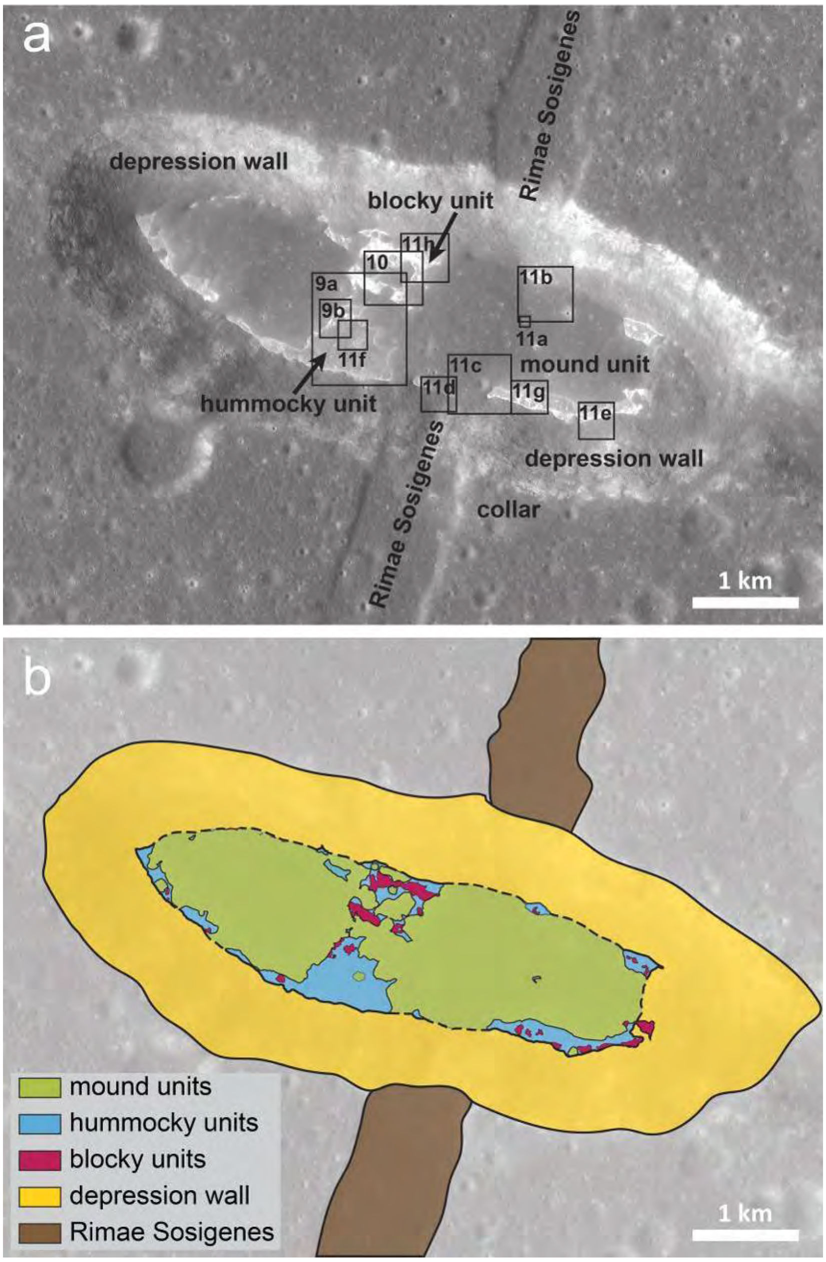

Fig. 6. Sosigenes depression and IMP. (a) LROC NAC (M1129354261) image of Sosigenes, incidence angle = ~46°, pixel size = ~1.2 m. Representative morphologic units are labeled. Locations of Figs. 9–11 are indicated by black boxes. (b) Geologic sketch map shows the distribution of the different morphologic units associated with the Sosigenes IMP.

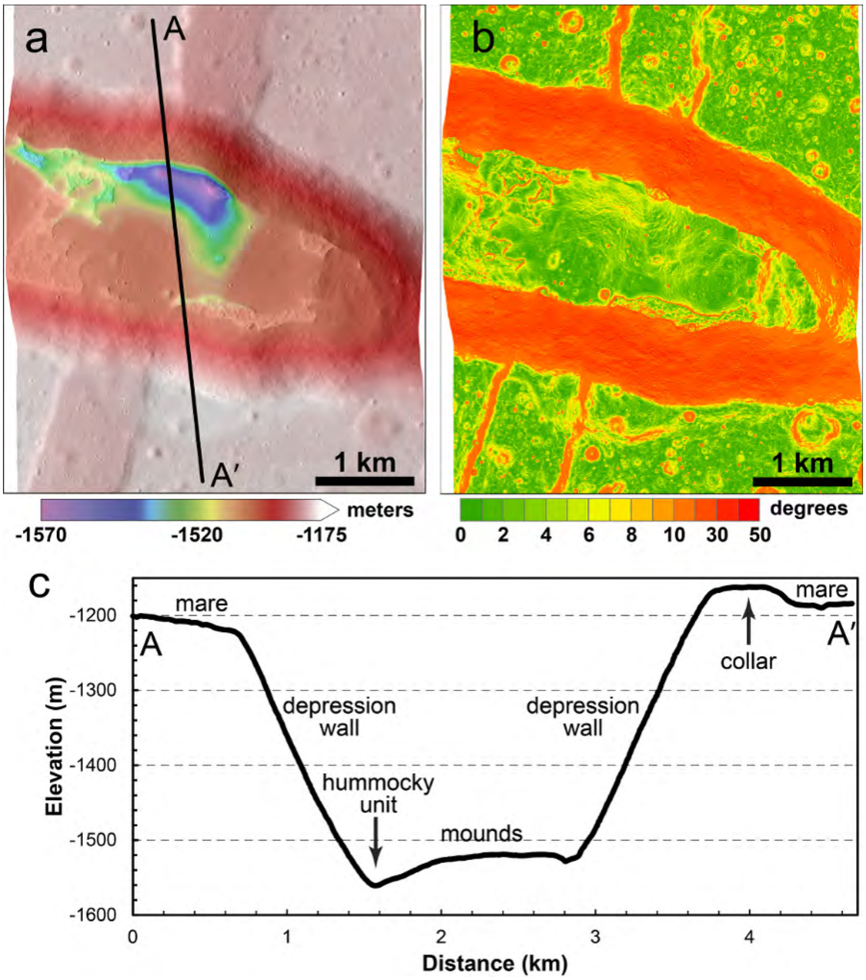

Fig. 7. Topography and slope of Sosigenes depression and IMP. (a) Color NAC DTM topography overlain on LROC NAC images (portion of frame M177508146). The DTM data are displayed with a two-component piecewise linear stretch (-1570 – -1520 m and -1520 – -1175 m) to highlight the topographic relief within the floor of the Sosigenes depression. The line shows the location of the topographic profile in (c). (b) Slope map, and (c) topographic profiles derived from LROC NAC DTM in (a). LROC NAC DTM topography is available at http://lroc.sese.asu.edu/.

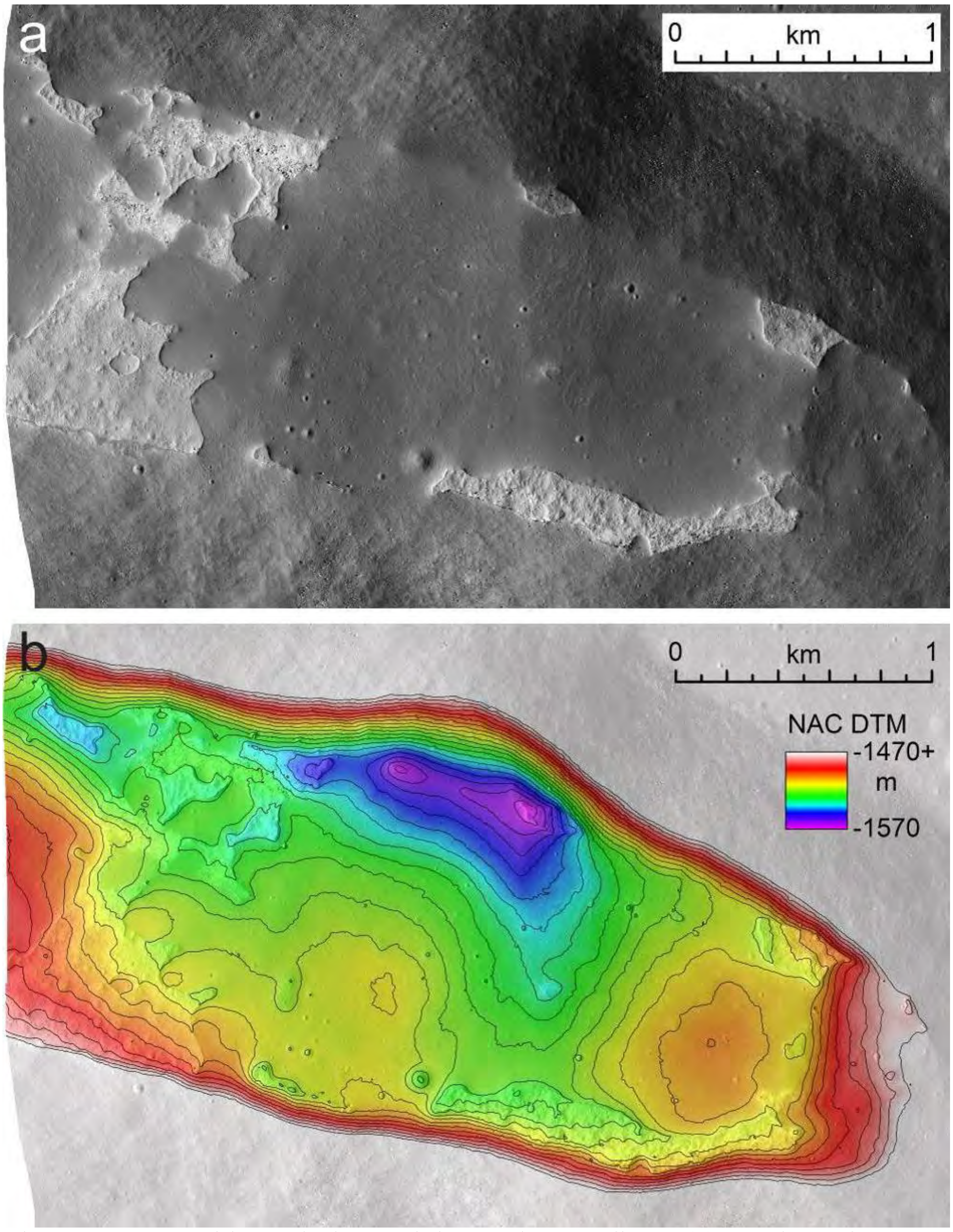

Fig. 8. Topographic variations of the Sosigenes floor. (a) Portion of LROC NAC NACM177514916. (b) Same area shown by color-shaded NAC DTM topography overlain on LROC NAC NACM177514916; contour interval is 5 m.

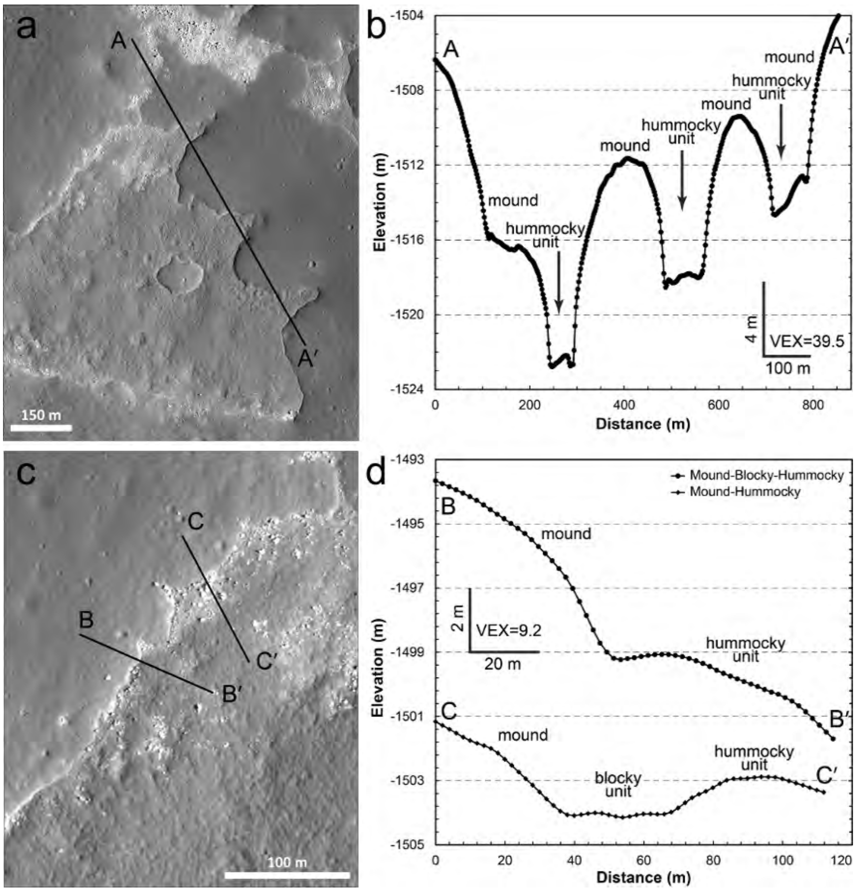

Fig. 9. (a) Contacts between mound and hummocky units near the center of Sosigenes, LROC NAC frame M177508146, 0.48 m/pixel. (b) Topographic profile across the mound and hummocky units shown in (a). Elevation is derived from NAC DTM data, 2 m/pixel. (c) Portion of LROC NAC frame M177508146R shows the contact between the mound and hummocky units, with some blocky materials present along the contact. (d) A NAC DTM-derived profile shows the topographic relief from mound, blocky to hummocky units (C-C’). For comparison, a profile directly crossing from the mound to the hummocky unit is also illustrated (B-B’).

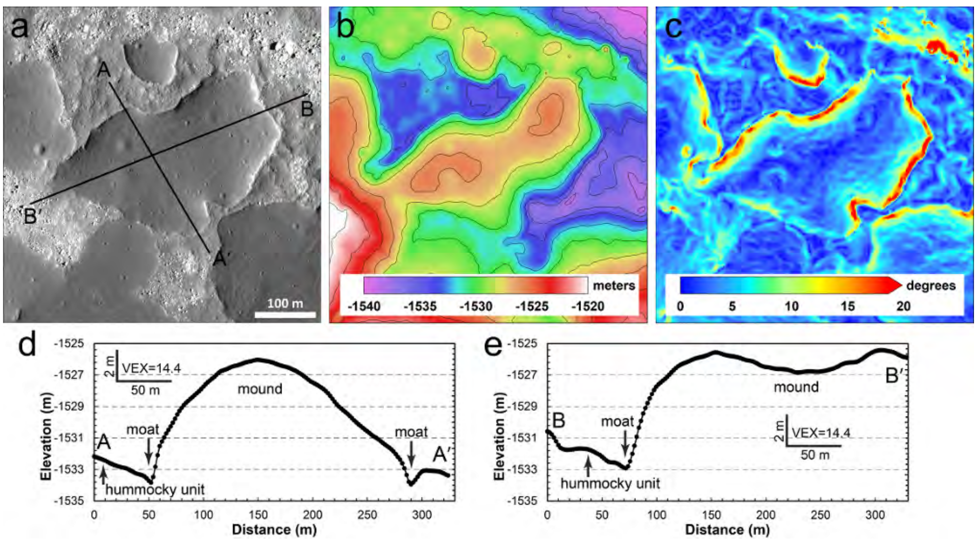

Fig. 10. Morphology and topography of an almost completely isolated mound on the floor of the Sosigenes pit crater. (a) Portion of LROC NAC frame M177508146, 0.48 m/pixel. Black lines show locations of topographic profiles in (d) and (e). (b) NAC

DTM topography with overlying 2 m interval contour. (c) Topographic slope map. (d and e) Topographic profiles derived NAC DTM data in (a).

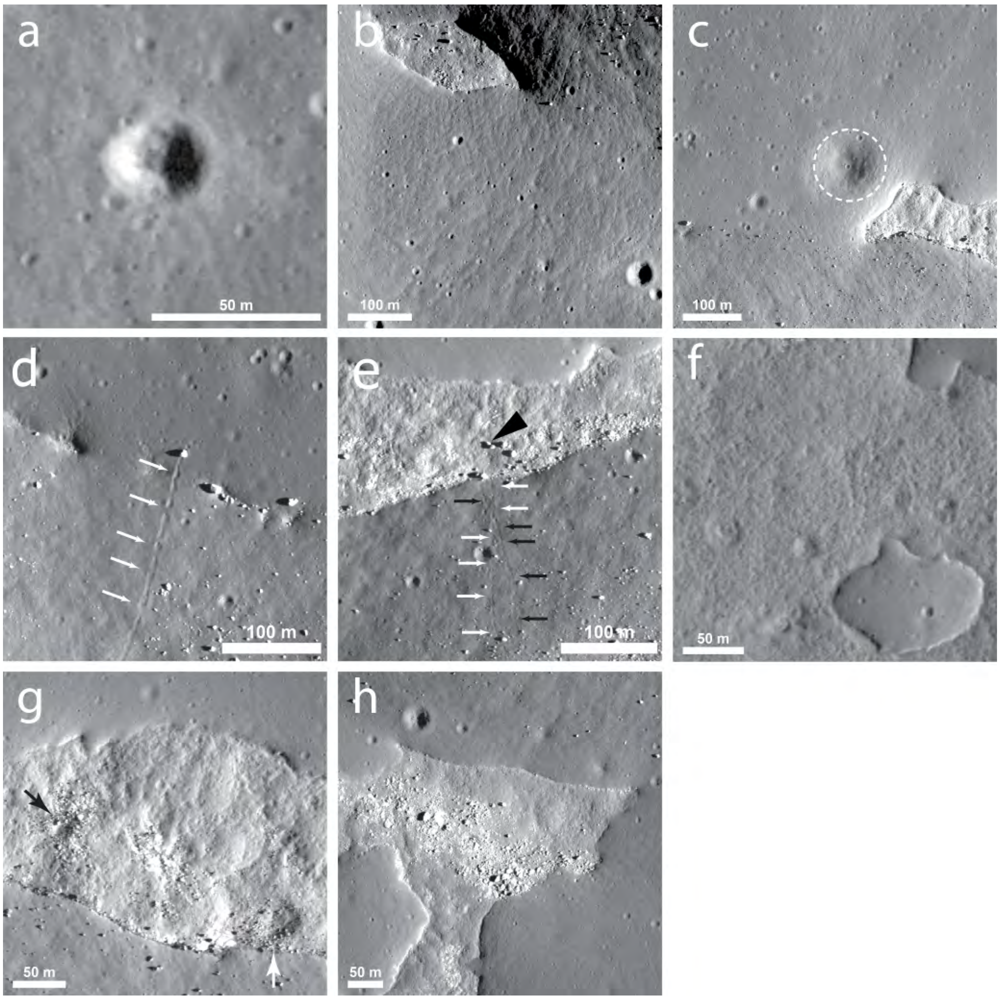

Fig. 11. Morphology of the Sosigenes IMP interior illustrated with LROC NAC images. (a) A fresh impact crater superposed on the mound units, with a diameter of ~30 m and a floor depth of 4.8 m (depth/diameter = ~0.16). (b) Elephant-hide textured regolith observed on the northern floor. (c) An impact crater with diameter of ~130 m (white dashed circle) superposed on the mound units. (d) A boulder trail (5–8 m wide, traced by white arrows) develops at the depression wall and extends to the mound units. The boulder (~8×8 m in dimension) rolls ~25 m on the mound units, and generates an obvious boulder trail (linear depression), indicating a layer of unconsolidated materials (meters thick) on the mound units. (e) A boulder trail (~3–6 m wide, traced by white arrows) originates from the wall slope but terminates at the contact between the wall and hummocky units of Sosigenes. However, no boulders which should be large enough to generate the trail (with dimension comparable with the width of the trail) are observed at the ending of the trail. A large boulder ~33 m from the contact (~6×4 m in size, marked by the black triangle) is a candidate for the rolling boulder, but it does not generate any resolved trails on the hummocky units where it crosses, indicating a very thin layer or even absence of mantling unconsolidated materials on the hummocky units. Another boulder trail (~4–7 m wide) is also observed (traced by the black arrows), which also terminates at the contact between the wall and the hummocky units, but a large boulder (~8×6 m in size) is found at the end of the trail. (f) Ridged and pitted surface texture of the hummocky

units. A small mound is present at the lower right corner of the panel. Many irregular depressions are also observed on the hummocky units. (g) Two small craters present on the hummocky units of Sosigenes; the diameter of the western crater (black arrow) is ~20 m, and the eastern one (white arrow) is ~35 m. (h) Blocky units surrounded by the hummocky units at Sosigenes; massive boulders are observed. Panels (a), (c), (f) and (g) are portions of LROC NAC frame M177514916, 0.52 m/pixel; panels (b), (d), (e) and (h) are portions of LROC NAC frame M177508146, 0.48 m/pixel. A raw resolution version of this figure is provided as supporting information.

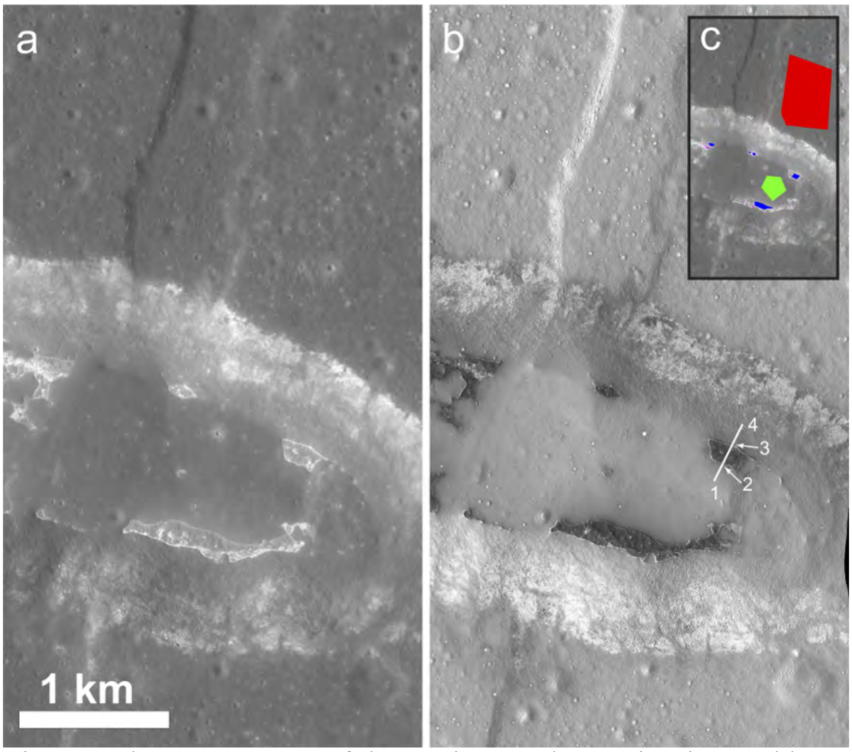

Fig. 12. The eastern part of the Sosigenes depression imaged by LROC NAC. (a) Portion of LROC NAC frame M1175290064L at 1.104 m/pixel resolution, α = 30.27°, stretched from a radiance factor value of 0.006 to 0.06. (b) Phase-ratio image, $f(30°)/f(67°)$, stretched from a phase ratio value of 1.1 to 1.8. The white line shows the locations where the phase ratio profile is derived in Fig. 15, and the numbers correspond to the numbers in Fig. 15. (c) Image regions of interest (ROIs) for evaluating the brightness and phase ratio values of different units: red = mare background (1,233,144 pixels), green = mound units (164,714 pixels), blue = hummocky units (47,975 pixels), magenta = blocky units (5,175 pixels). A raw resolution version of panel c is provided as supporting information.

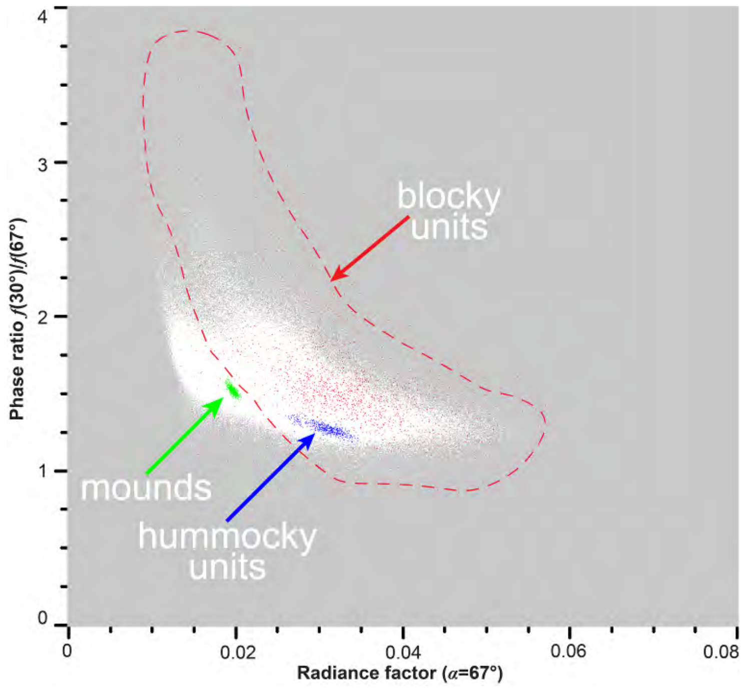

Fig. 13. Two-dimensional scatter plot of phase ratio $f(30°)/f(67°)$ and radiance factor $f(67°)$, for western part of Fig. 12. Locations of typical morphological terrains within Sosigenes interior are marked: green points (mounds), blue points (hummocky units) and magenta points (blocky units). A very weak correlation is observed for the whole plot, and the Sosigenes interior morphological units are generally not in line with the background pixels.

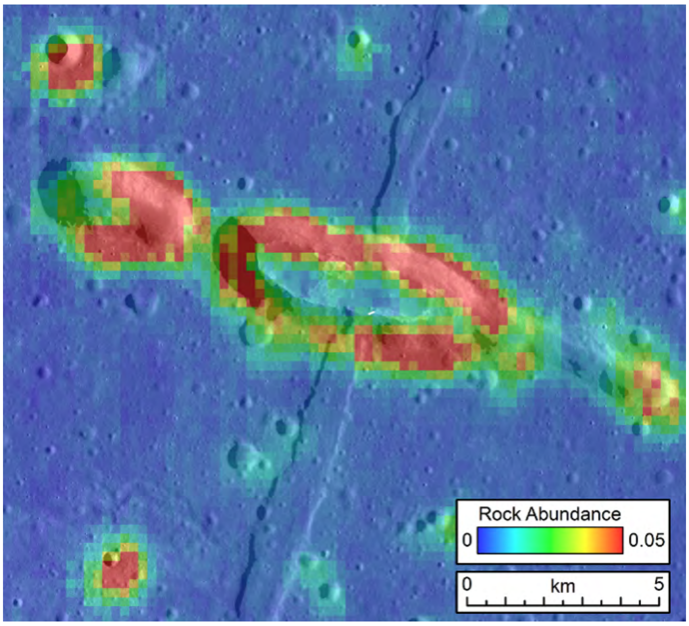

Fig. 14. Diviner rock abundance (areal fraction of each scene occupied by exposed rocks ~1 m or larger) in color overlain on Kaguya TC evening image mosaic.

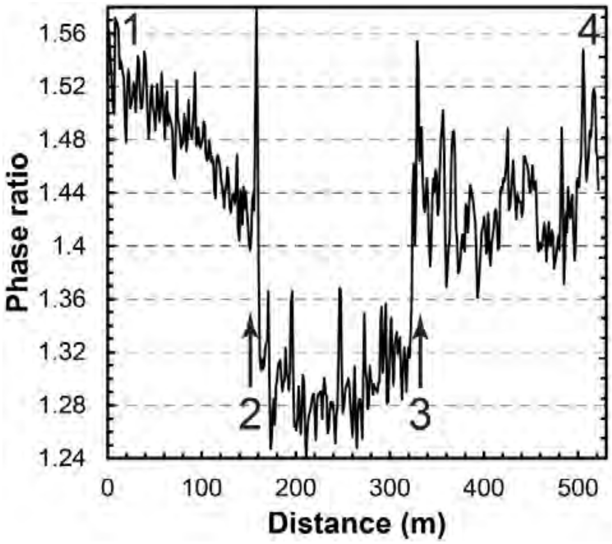

Fig. 15. Phase ratio profile derived from the $f(30°)/f(67°)$ image of Sosigenes (Fig. 12b). The location of the profile is marked by the white line and corresponding numbers in Fig. 12b.

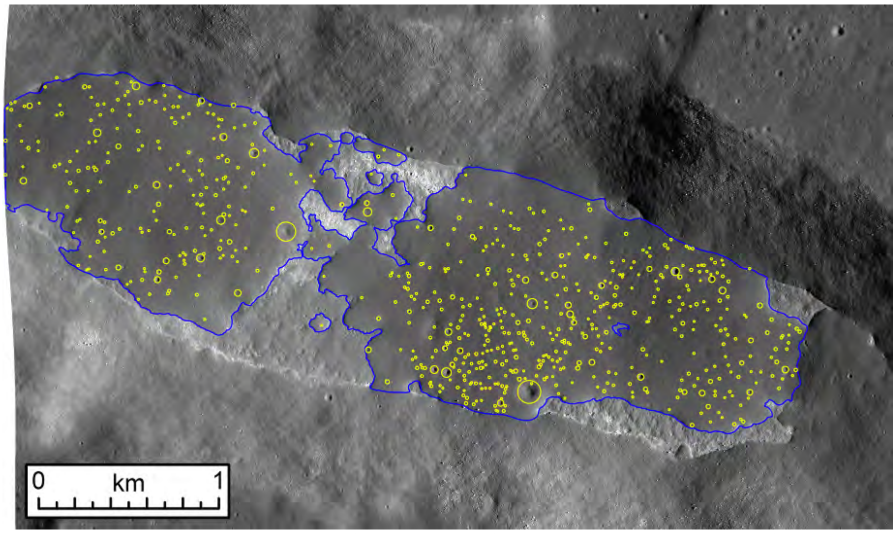

Fig. 16. Impact craters (with estimated rim positions marked by yellow circles) accumulated on the mound units of the Sosigenes IMP; the background image is a portion of LROC NAC frame M192824968R. A raw resolution version of this figure is provided as supporting information.

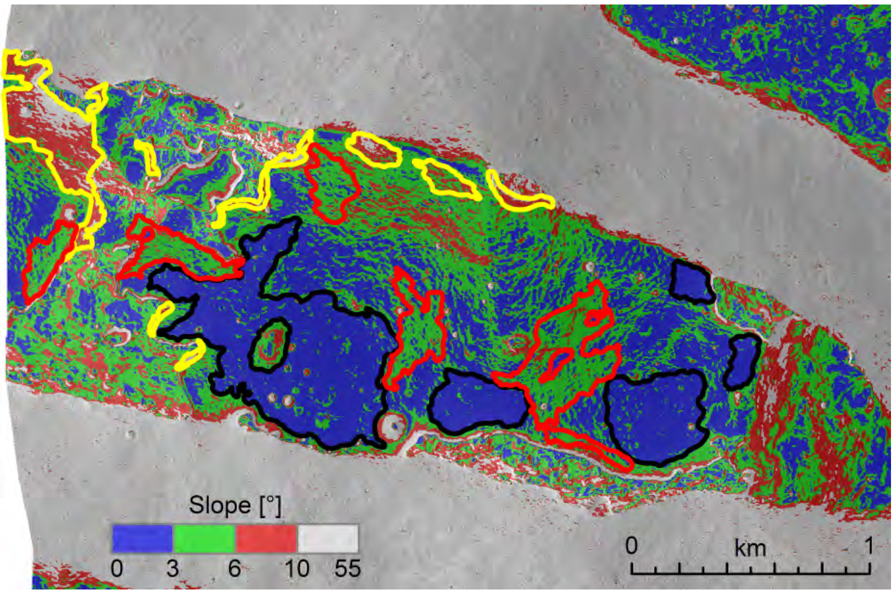

Fig. 17. NAC DTM slope map for the Sosigenes depression floor. In order to highlight the slope variation of the Sosigenes mounds, the color ramp is concentrated in the 0–10° slope range. Several patches with representative topographic slopes are outlined for investigating the potential correlation between crater density and regional slope: black outlines for relatively flat areas (<3°), red for medium-sloped areas (dominantly ~3–6°), and yellow for relatively steep areas (dominantly >6°). See Fig. 18 and Table 4 for the analysis results.

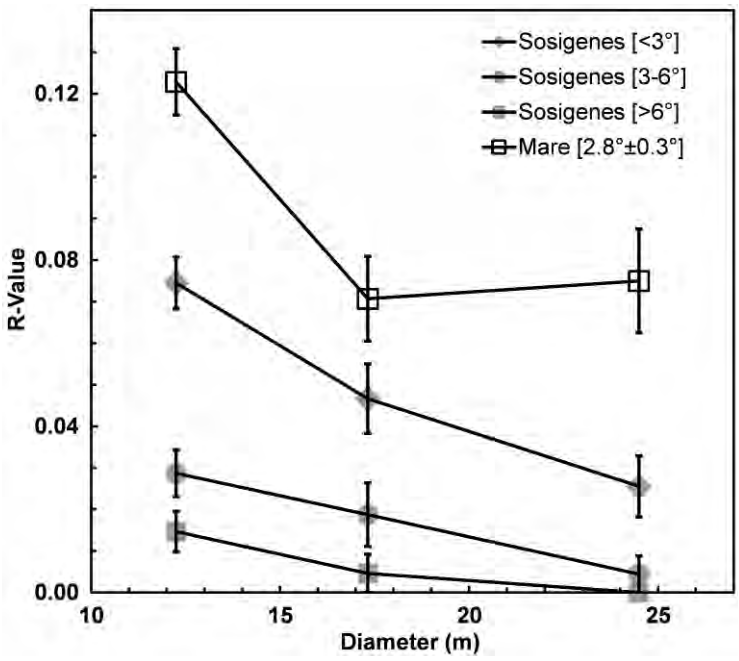

Fig. 18. Plot of CSFD (R-values) with several crater diameter range (10–15 m, 15–20 m, and 20–30 m) for representatively-sloped areas in Sosigenes mounds outlined in Fig. 17 and surrounding mare region outlined in Fig. 20 (white square). See Table 4 for the detailed values.

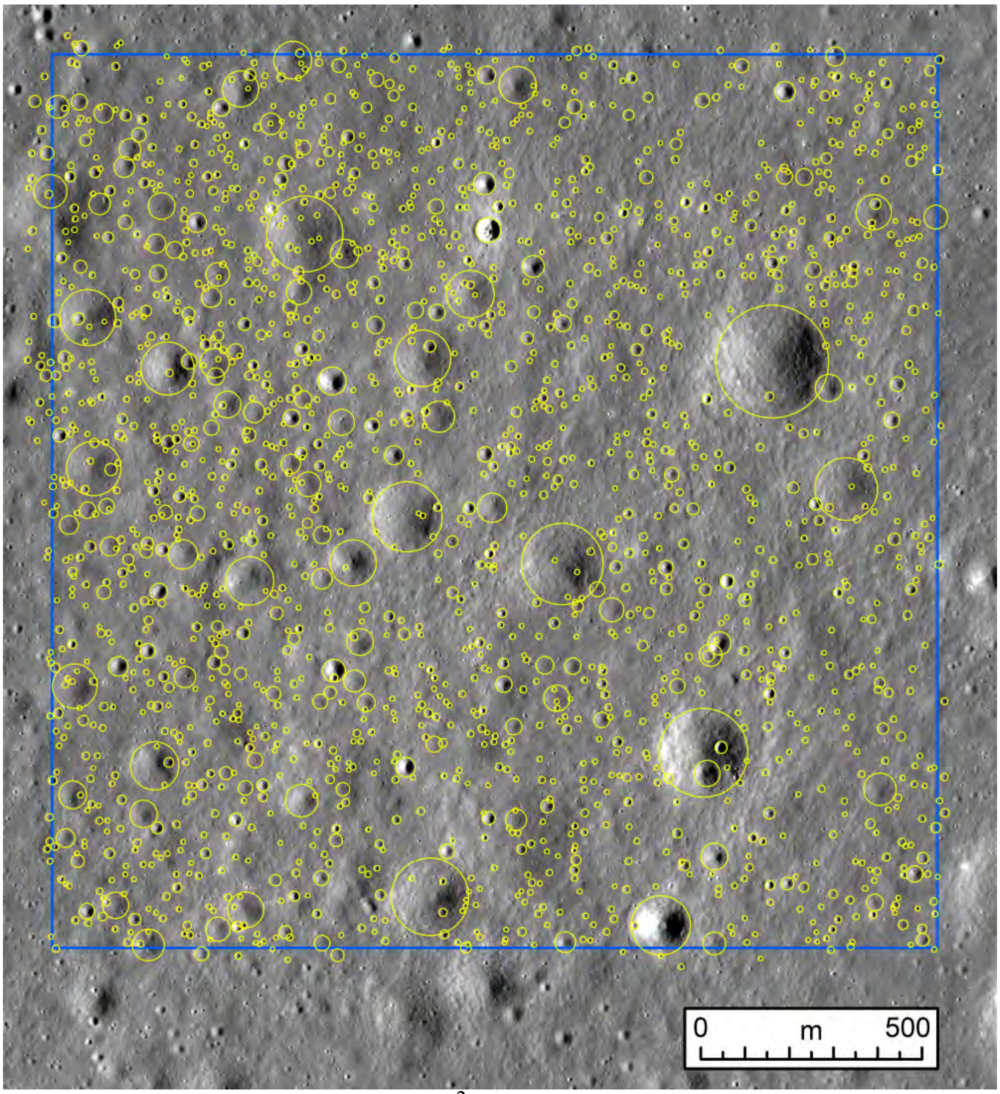

Fig. 19. Crater counts for a 2×2 km^2 square mare area south Sosigenes IMP. The location of this panel is shown as the white box in Fig. 2a. A raw resolution version of this figure is provided as supporting information.

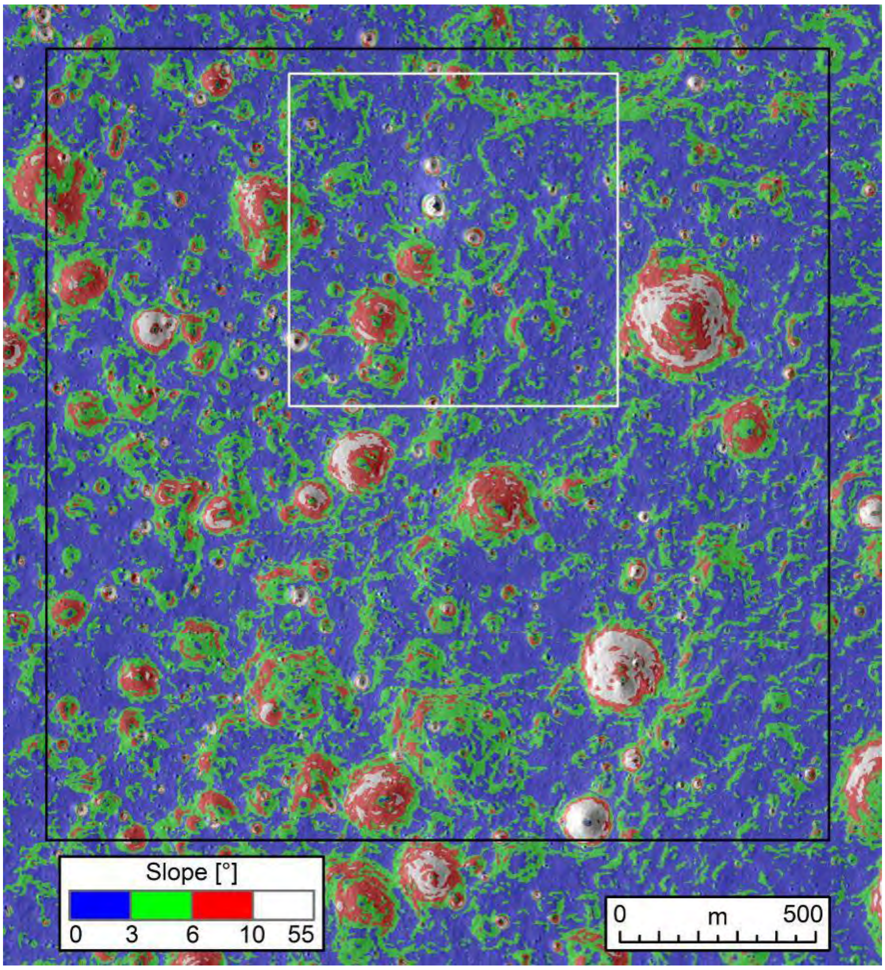

Fig. 20. NAC DTM slope of the mare crater-counting area (black square); the white square is the area where crater density-topographic slope correlation is analyzed (Fig. 18 and Table 4).

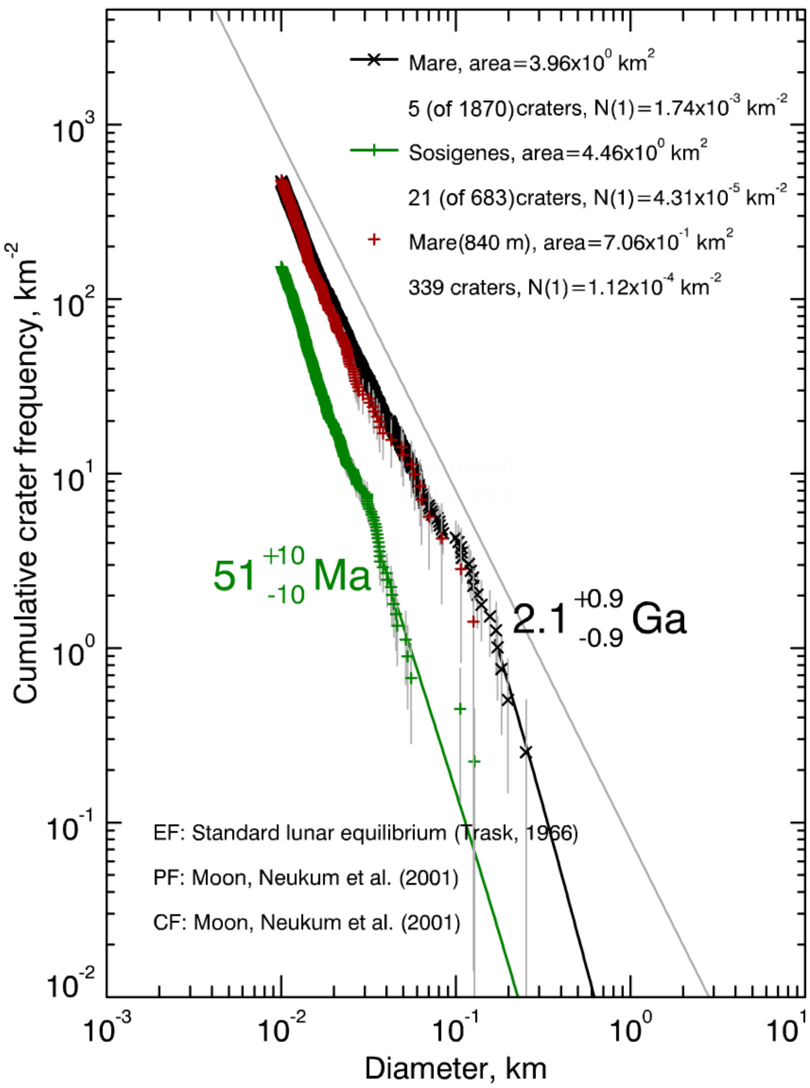

Fig. 21. Cumulative size frequency distribution of impact craters superposed on the Sosigenes mounds (green crosses), surrounding mare 2×2 km^2 area (black ‘×’s), and 840×840 m^2 sub-area (red crosses, for slope effect investigation). The gray line on the right is the lunar equilibrium function (EF) curve from Trask (1966). The model age fitting is based on production function (PF) and chronology function (CF) from Neukum et al. (2001), using the CraterStats software package (Micheal and Neukum, 2010).

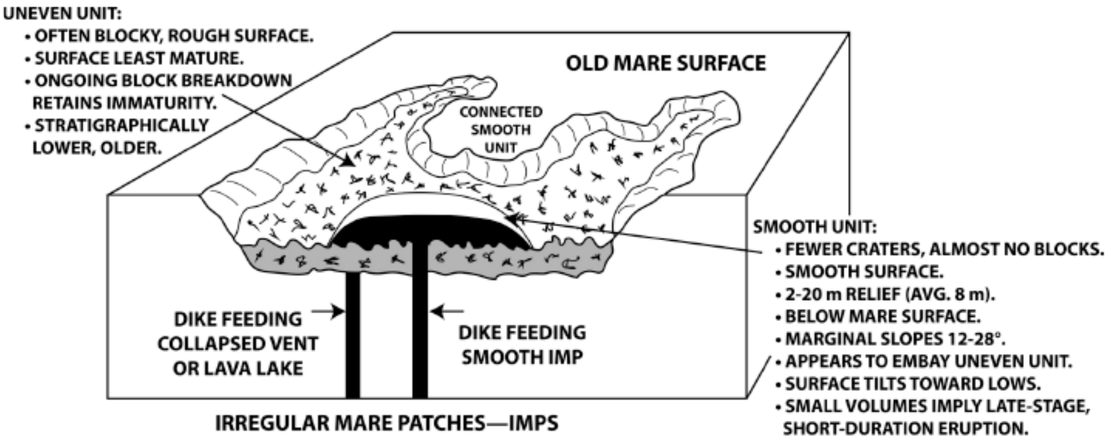

Fig. 22. Block diagram illustrating the major characteristics of the irregular mare patches, and highlighting the interpretation of Braden et al. (2014) that the floor and mounds represent very late-stage extrusions (<100 Ma) compared with the surrounding ancient mare basalts (~2–3 Ga in the case of Ina and Sosigenes). In the Braden et al. (2014) interpretation, the floor units and mounds are both extremely young, but the mounds postdate the floor units. In the interpretation of Garry et al. (2012), the mounds are inflated lava flows and the rough floor units extrude from the base of the inflated flow. In the interpretation of Schultz et al. (2006) the anomalously young ages (<10 Ma in the case of Ina) are caused by deep-seated gas release that elutriates, blows out and ejects the fines, causing the observed rough, immature and blocky/hummocky floor units. In our interpretation, the rough floor units are the surface of a lava lake and the mounds are extrusion of late-stage magmatic foams. The young ages are attributed to the unusual properties of the magmatic foam and the solidified micro/macrovesicular lava lake.

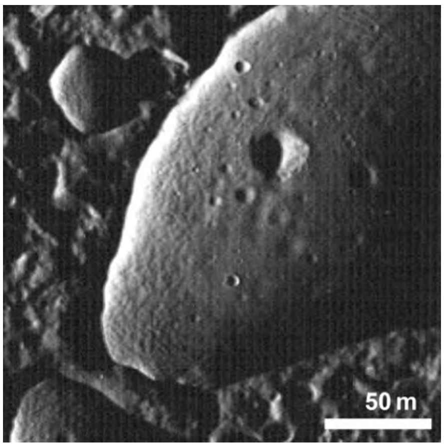

Fig. 23. Depressions at the Ina mound summits. LROC NAC M132800178, ~0.57 m/pixel, incidence angle=~87.2°. The largest depression is the same one shown in Fig. 4d of Garry et al. (2012).

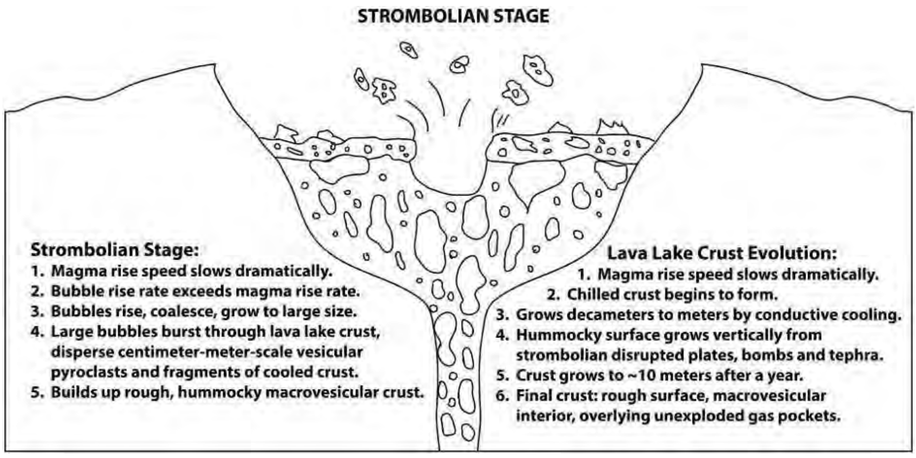

Fig. 24. Diagram (from Fig. 3 in Wilson and Head 2017b) illustrating processes operating in the waning stages of an eruption in Sosigenes pit crater: the strombolian-style eruption phase of lava lake evolution (left text) and development of the lava lake crust (floor hummocky/blocky units) (right text).

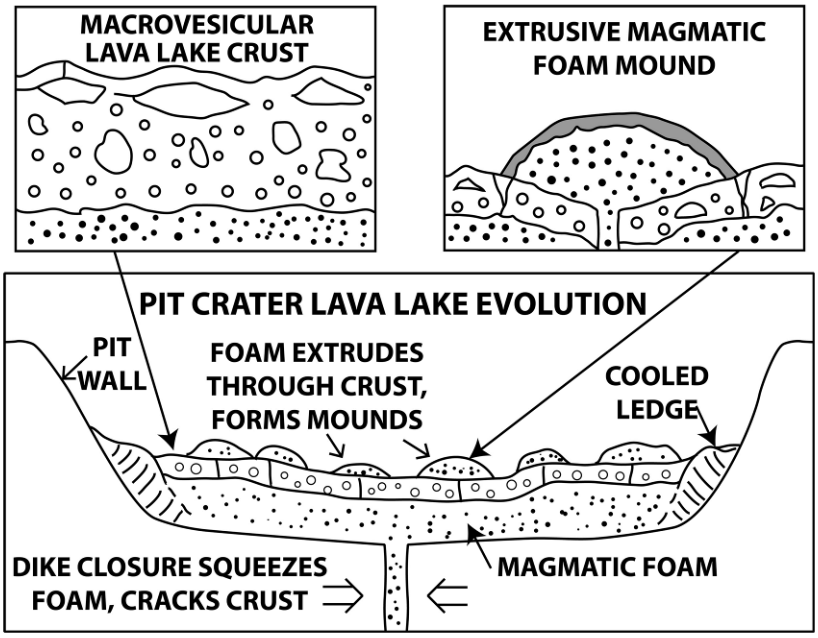

Fig. 25. Cross section (from Fig. 3 in Qiao et al. 2017) of magmatic foam emplacement during the final stage of eruption process in the Sosigenes pit crater.

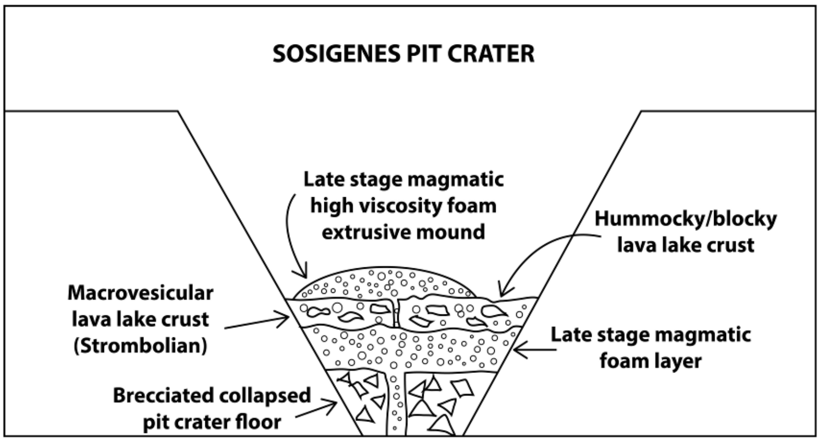

Fig. 26. Cross section of the final products of waning stage of eruptive processes in the Sosigenes pit crater.

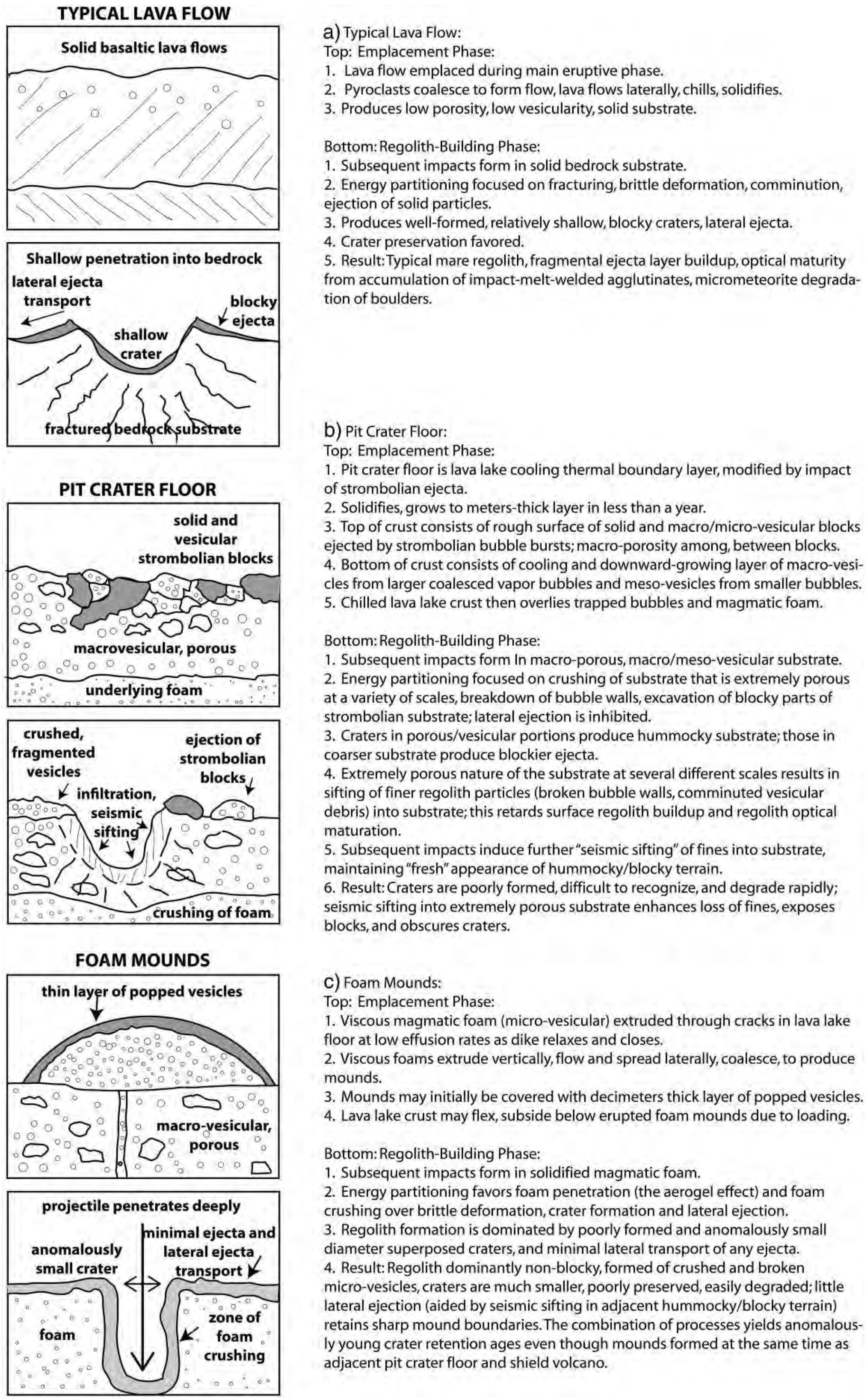

Fig. 27. Block diagrams (from Fig. 9 in Wilson and Head 2017b) illustrating the substrate characteristics (top) of (a) normal basaltic lava flows, (b) lava lake crusts

and (c) extruded foam mounds. Bottom panels and texts of each diagram (a–c) show the nature and results of post-emplacement impact cratering, regolith formation and landscape evolution operating on their surfaces.

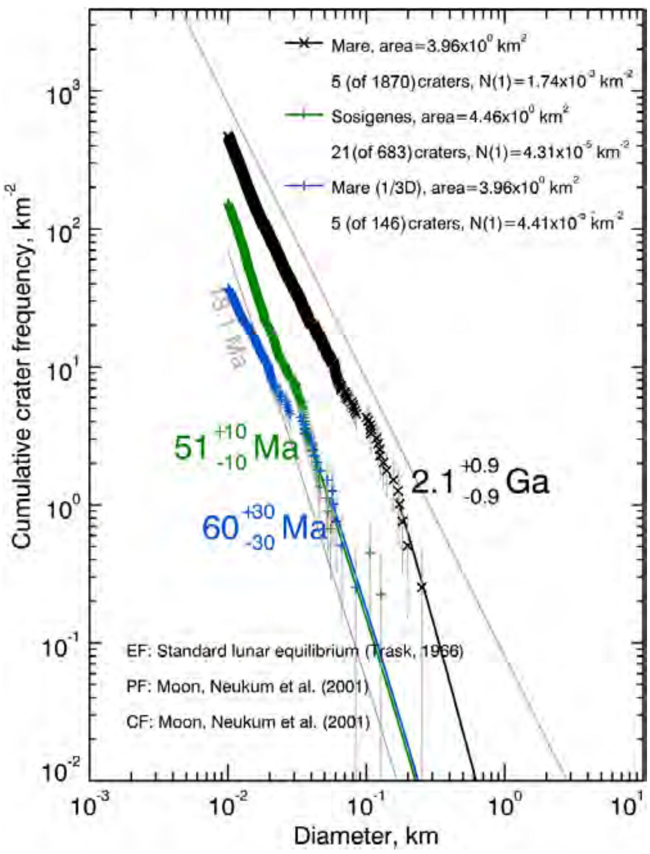

Fig. 28. The effects of cratering a highly porous target (magmatic foam of the mounds) on the crater retention ages. The original crater size frequency distribution of the 2×2 km surrounding mare region is plotted as black '×'s. All the craters counted on the mare are scaled with a factor of three diameter decrease (plotted as blue crosses); this produces a similar CSFD to the Sosigenes mounds (green crosses), and yields a model age of <100 Ma. The gray line on the right is the lunar equilibrium curve from Trask (1966), and the left gray line is the isochron for the 18.1 Ma age reported by Braden et al. (2014).